Management of Conjugate Heat Transfer Using Various Arrangements of Cylindrical Vortex Generators in Micro-Channels

Muhammad F. B. Raihan[a], Mushtaq T. Al-Asadi*[a, b], H. M. Thompson[a]

[a]*Institute of Thermofluids, School of Mechanical Engineering, University of Leeds, UK*

[b]*Engineering Audit sec., Business development Dpt., Basra Oil Company, Ministry of Oil, Basra, Iraq.*

Abstract

Placing cylindrical vortex generators (VGs) at the base of a uniform micro-channel heat sink (MCHS) enhances the heat transfer, but incurs a substantial pressure drop. The effect of different VG parameters, including position (front, middle or back), radius (R) in the range of (100-300) μm and distance (D) between them (0-500) μm are considered to enhance the conjugate heat transfer. Laminar flow and heat flux conditions relevant to microelectronics water cooling systems (100 W/cm^2) are used. The numerical approach, using COMSOL Multiphysics® software, is validated and found to be in good agreement against benchmark experimental and numerical studies. It is generally found that VGs enhance heat transfer but that the pressure drop increases. The lowest thermal resistance is achieved when placing VGs at the front of the MCHS with no distance between them and R=300 μm, but this also results in the highest pressure penalty. Results also show that it is not necessarily the best heat transfer enhancement that leads to the highest thermal-hydraulic performance (PEC) index. The highest PEC index is achieved at the front position, with R=100, D=0μm and Re > 250.

Keywords: Thermal-hydraulic performance (PEC), Micro-scale cooling system, Thermal management, Vortex generators position, pressure drop reduction.

---

*Corresponding author, email:
mushtaq@boc.oil.gov.iq (M. T. Al-Asadi).

Nomenclature

A_s	surface area of the whole heat sink (μm^2)
CFD	Computational Fluid Dynamics
C_p	Specific heat, J/Kg.K
D	Distance between VGs, µm
FEM	Finite Element Method
K	Thermal conductivity, W/m.K
L	Channel length, µm
VGs	Vortex generators (VGs)
ΔP	Pressure Drop, N/m^2
q	Uniform heat flux, W/cm^2
MCHS	Micro-Channel Heat Sink
R	Radius of VGs, µm
Re	Reynolds number
T	Temperature, K
X	Axial distance, µm

Greek Symbols

μ	Viscosity, Pa.s
θ	Thermal resistance, K/W
ρ	Density, kg/m^3

Subscripts

ave	Average
In	Inlet
max	Maximum
Out	Outlet
S	Surface
s	Solid
L	Liquid

1. Introduction

Effective thermal management in electronic micro-chips is crucial since the excessive heat generated can cause damage to the micro-chip components [1]. Inexorable reductions in the size of the components and increases in processor power makes it even more challenging for thermal researchers to produce an effective cooling method and/or a design to remove the generated heat.

Researchers have made several important discoveries about the potential of using air and liquid cooling to remove heat effectively from the micro-system [2]. Different methods of cooling have been introduced such as micro-jet impingement, thermo-electron coolers, forced air cooling, micro-heat pipes, micro-electro-hydrodynamics, and micro-channel heat sinks (MCHSs) [3-5]. The best method of cooling discovered from these methods is to use MCHS due to its higher surface area to volume ratio value [2]. One of the earliest MCHS systems used an air-cooled system, but due to increasing rates of energy dissipation required, different working fluids have been used (i.e. nanofluids or ionic liquids) to provide more effective heat removal systems, albeit with a high pressure penalty [6-13]. Interestingly, even though the overall enhancement (Performance Evaluation Criteria (PEC) index) is not significant, this has motivated researchers to investigate the possibility of implementing advanced fluids that have high thermal properties in heat transfer systems. For example, the PECs for nanofluids are often poor (with PEC < 1) [1], but they are still attracting researchers to investigate the heat transfer enhancement neglecting the pressure penalty[14].

It is necessary to enhance the heat transfer rate of MCHS due to the rapid developments of micro-chips whilst avoiding infeasible growth in the associated pressure drop. One potential method, which is examined here, includes adding extra geometry (extended surface area) to the channel which is called a vortex generator (VG). VGs were first introduced in 1969 by Johnson and Joubert for heat transfer improvement [15]. VGs come in different shapes including wings, winglets, blocks, protrusions, fins and ribs [16-22]. The goal of a VG is to disturb the flow in the channel to improve heat transfer performance. The disturbed flow will create vortices which can be categorised into transverse and longitudinal vortices [23, 24]. A transverse vortex has its rotation axis at a right angle to the direction of flow and a longitudinal vortex has it parallel to the direction of flow [25-29]. The installed VG can be either at the bottom or on the side walls of the MCHS or both. The effective use of VGs has led to significant improvements in the heat transfer performance of micro-channels [27]. For instance, Wong and Lee [30] found that heat transfer was enhanced by placing triangular ribs in the transverse micro-chamber and concluded that incrementing the width and the height of the ribs improves heat transfer, while increasing the pressure drop [12].

Ebrahimi et al. [18] and Datta et al. [24] considered inclined longitudinal VGs (LVGs) within a straight rectangular micro-channel heat sink. From their findings, vortices size increases with increasing LVG angle and Reynolds number. As the size of vortices increases, the convective heat transfer increases since there is continuous breaking of the boundary layer and flow re-initialisation. But this enhanced rate of heat transfer is at the expense of a large pressure drop. Samadifar and Toghraie [31] introduced six new type of VGs on fin-plate heat exchangers using triangular channel profiles. From their results, the simple rectangular VG (SRW) has the highest rate of heat transfer with 7% increment compared to other five VGs shapes. All VGs shapes studied show an increase in pressure drop within the channel. Convective heat transfer is increased as the height of VGs increased. For a 45° angle of attack of VG, the highest overall performance achieved.

Khoshvaght-Aliabadi et al. [32] used longitudinal spacing among delta-winglets VGs in straight channels. They stated that the heat transfer coefficient is enhanced by 50% using two side cuts and four delta-winglets and a high to low (HL) arrangement compared to a smooth channel. The use of the HL arrangement shows a great increase in heat transfer coefficient while the Low to High (LH) arrangement shows an increase in pressure drop. The pressure drop is greatly influenced by the number of delta-winglets used. Overall hydrothermal performance is achieved when using the one side cut and one delta-winglet configuration and uniform (U) arrangement as well as the HL arrangement with two side cuts and two delta-winglets. Lu and Zhai [33] utilised winglet-type VGs with dimples in their micro-channel heat sink. Five different configurations tested were smooth micro-channel, micro-channel with only VGs, micro-channel with only dimples, micro-channel with both dimples and VGs – "common flow up" and "common flow down". Their results showed that using dimples and VGs induces significant improvement in heat transfer with a lower pressure penalty. The "common flow up" and "common flow down" configurations of VGs shows an improvement in heat transfer when they are used together with dimples with a 2.4-4.7% enhancement. The "common flow down" shows better performance in heat transfer compared to the "common flow up" configuration. Li et al. [34] used VGs to increase the thermal performance of pin-fin heat sinks. Increasing the height of VGs results in a decrease in thermal resistance. Using the common-flow-up configuration gives lower thermal resistance compared to the common-flow-down configuration. An angle of attack of 30° give the best overall performance for both thermal resistance and pressure drop. Setting the shortest distance between VG would also give the best thermal-hydraulic performance of heat sink. From this work, only a small thermal resistance enhancement is achieved while there is a very large pressure drop increase.

Li et al. [35] used rectangular VGs combined with triangular cavities on the side walls and achieved improved heat transfer performance due to the fluid mixing from the flow disturbance and the formation of a hydrodynamic layer. As the width increases, the friction factor and Nusselt number are improved. The heat transfer enhancement factor improved by 1.61 when using cavity and rib widths of 0.3 and 2.24, respectively, at a Reynolds number of 500 compared to conventional MCHS. Khoshvaght-Aliabadi et al. [36] utilised plate-fin heat exchanger (PFHE) with VGs. They concluded that, rectangular wings enhance the performance of heat transfer by 58.3% compared to PFHE without wings. The pressure drop values increases when wings' pitch and height decrease and wings' width, channel length and angle of attack increase. The wings' height and angle of attack has the most significant effect on the performance evaluation criteria. Chai et al. [37] compared five shapes of sidewall ribs (forward triangular, backward triangular, equal triangular and semi-circular) inside a rectangular channel. Enhancement of heat transfer was achieved using ribs but with a higher pressure drop penalty. The results showed the circular ribs to have the lowest thermal resistance compared to other VG shapes.

Considering the use of cylindrical VGs, Al-Asadi et al. [26] confirmed that the semi-circular VGs offered the lowest thermal resistance compared to the other shapes when VGs were placed at the bottom of the channel. Al-Asadi et al. [27] investigated subsequently the influence of cylindrical VGs and reported that cylindrical VGs (half-cylinder and quarter-cylinder VGs) increase MCHS performance. The radius of the VGs (0-400 μm) and the heat flux were varied in the study with Re ranging from 100 to 2300. It was found that half-circle VGs are more effective than quarter-circle VGs for heat transfer improvement. The half-circle VG resulted in lower pressure drop compared to the quarter-circle VG. Moreover, Al-Asadi et al. [23] thoroughly studied three different models of placing the VG for full span, centred and split configurations. The results showed that the centred VG offered better heat transfer improvement compared to the other two models with an optimum number of VGs (5 circular VGs).

Using VGs offered heat transfer enhancements, however, the pressure penalty was increased. Thus, the literature has shown a gap of knowledge in how to enhance the heat transfer in micro-channel heat sinks (MCHSs) while controlling the increase in pressure drop. This point has motivated researchers to propose novel ways in which heat transfer can be enhanced while trying to reduce the increase in pressure drop and one promising alternative is to employ cylindrical vortex generators (VGs) [23]. To the best of the authors' knowledge, there is currently a significant knowledge gap on how VGs distribution can be used to provide effective thermal management by enhancing heat transfer while controlling the increase in pressure drop. Therefore, this study proposes a simple geometrical modification to mitigate the increase in pressure drop when using VGs in micro-channels. From the reviewed literature, it can be seen that having very small thermal resistance reduction while having very large pressure drop increase can reduce the effectiveness of heat sinks [34, 38], this will be discussed further in **Section 5.3** regarding the PEC index analysis.

This study extends a series of publications [23, 26, 27, 37], to explore the influence of different positions of VGs (at the front, middle and back) and determine the optimum radius, R, and distance between VGs, which have not been considered previously. These changes will be beneficial by enhancing the heat transfer and reduce the increase in pressure drop simultaneously. The paper is organised as follows. The problem specification is given in **Section 2**. The 3-D computational method (conjugate heat transfer model, boundary conditions and heat transfer performance) are described in **Section 3**. A mesh independence study is presented in **Section 4**. The results and discussion and conclusion are given in **Section 5** and **Section 6** respectively.

2. Problem Specification

The geometry of the MCHS has the dimensions given in Table 1, and a base area of 25 x 10^8 µm^2 as shown in **Fig. 1 (A1)**. To compare the performance of the modified MCHS, a baseline micro-channel is constructed as a guideline (**see Fig. 1 (B)**). The MCHSs have VGs added at the bottom of the micro-channel. The channel is divided into 3 equal lengths of front, middle, or back which act as a full channel where the VGs are positioned evenly in each division (**see Fig. 1 (D)**). The VGs are placed only in one division at a time for analysis in this study and not simultaneously between divisions. Each division has five VGs, each with a range of radii, R, and rib distances, D.

3. Computational method

3.1 Conjugate heat transfer model

The model of the MCHS employs a number of simplifying assumptions. The flow of water is considered as laminar, steady, and Newtonian and to have a temperature-dependent density and viscosity [23, 26, 39]. Gravitational effects are neglected in such a small domain with forced convection. The 3D velocity of water $\boldsymbol{u} = (u, v, w)$ in the (x, y, z) cartesian coordinate directions with p, ρ and μ the pressure, density and the viscosity of the liquid respectively. The governing equations used are the continuity and Navier-Stokes equations:

$$\nabla \cdot \boldsymbol{u} = 0 \quad (1)$$

$$\rho(T)(\boldsymbol{u} \cdot \nabla)\boldsymbol{u} = \nabla \cdot \left[-p\boldsymbol{I} + \mu(T)(\nabla\boldsymbol{u} + (\nabla\boldsymbol{u})^T) - \frac{2}{3}\mu(T)(\nabla \cdot \boldsymbol{u})\boldsymbol{I}\right] \quad (2)$$

For the liquid phase, the energy equation is as follows:

$$\rho C_p \boldsymbol{u} \cdot \nabla T_L = k\nabla^2 T_L \quad (3)$$

where C_p, T_L, and k are respectively the specific heat, temperature, and thermal conductivity of the liquid. Conduction in the solid is modelled by:

$$\nabla \cdot (k_S \nabla T_S) = 0 \quad (4)$$

where T_S and k_S are respectively the temperature and thermal conductivity of the solid.

The ρ, μ, C_p and k are temperature dependent and are defined as follows [23, 26, 39]:

$$\rho(T) = 838.466135 + 1.40050603T - 0.0030112376T^2 + 3.71822313 \times 10^{-7}T^3$$

$$\mu(T) = 1.3799566804 - 0.021224019151T + 1.3604562827 \times 10^{-4}T^2 - 4.6454090319 \times 10^{-7}T^3 + 8.9042735735 \times 10^{-10}T^4 - 9.0790692686 \times 10^{-13}T^5 + 3.8457331488 \times 10^{-16}T^6$$

$$C_p(T) = 12010.1471 - 80.4072879T + 0.309866854T^2 - 5.38186884 \times 10^{-4}T^3 + 3.62536437 \times 10^{-7}T^4$$

$$k(T) = -0.869083936 + 0.00894880345T - 1.58366345 \times 10^{-5}T^2 + 7.97543259 \times 10^{-9}T^3$$

The Reynolds number, Re, is given by:

$$Re = \frac{\rho_f U_{in} D_h}{\mu_f} \tag{5}$$

where μ_f and ρ_f are the viscosity and density of the fluid respectively while U_{in} is the inlet fluid velocity and D_h as the hydraulic diameter given by $\left(D_h = \frac{4A_{ch}}{P_w} = \frac{2(W_{ch}.H_{ch})}{W_{ch}+H_{ch}}\right)$ where P_w, A_{ch}, W_{ch} and H_{ch} are the wetted perimeter, microchannel cross-sectional area, width and height of the channel respectively. The inlet velocity, U_{in}, is varied using different Reynolds numbers, Re, while the other parameters of μ_f, ρ_f and D_h are constant.

3.2 Boundary conditions

A single channel with symmetry conditions applied on the side is used to minimise the computational time. The symmetry conditions are applied for both the liquid and solid phases. At the top, front and back solid faces of the MCHS adiabatic conditions are imposed while at the base of the MCHS a uniform heat flux is applied at the bottom of the micro-channel as presented in **Fig. 1(B and D)** using $(-\boldsymbol{n}.(-k_s \nabla T) = q/A_h)$ where $\boldsymbol{n}$ represents the outward normal vector on domain boundary. At the MCHS inlet, the temperature is set to be 293.15K and velocity inlet normal to the boundary while the outlet pressure is set to be 0 Pa (gauge pressure at atmospheric pressure as the flow is assumed to exit the MCHS into an ambient atmosphere). A no slip velocity boundary condition is applied to the solid walls ($u_s = 0$), where u_s is the liquid velocity at the solid boundaries of the micro-channel with wall temperatures defined as $T_s = T_{f\ at\ wall}$ where T_s is the solid temperature and $T_{f\ at\ wall}$ is the fluid temperature at the wall. For the liquid-solid boundaries, the conductive and convective heat transfer to the fluid are coupled using the continuity of heat flux between the fluid and solid wall interfaces (refer to **Fig. 1 (D)**) where $T_{f,\Gamma}$ and $T_{s,\Gamma}$ are the interface temperatures of the liquid and the solid [40].

3.3 Heat transfer performance

The rate of heat transfer is measured using the average thermal resistance, θ, defined as:

$$\theta = \frac{T_{w,avg} - T_{in}}{A_s q} \quad (6)$$

where $T_{w,avg}$ is the average MCHS base temperature, T_{in} is the water inlet temperature, q is the heat flux applied to the base of heat sink and A_s is the MCHS base surface area.

Pressure drop, ΔP is calculated using the following formula:

$$\Delta P = P_{in} - P_{out} \quad (7)$$

where P_{in} and P_{out} are the inlet and outlet pressure.

To measure the overall performance of the MCHS, the θ and ΔP are included together in one equation called the Performance Evaluation Criteria (PEC) [23, 26]. These parameters are equivalent to the Nusselt number and hydraulic measurement. The PEC index is defined as follows:

$$\mathrm{PEC} = \frac{\theta_{\mathrm{s}}/\theta}{(\Delta P/\Delta P_s)^{1/3}} \quad (8)$$

where ΔP and θ are the ΔP and θ in a micro-channel containing VGs, and ΔP_s and θ_s are the same quantities in the corresponding uniform (i.e. uniform) micro-channel.

4. Numerical method

Equations (1) - (4) are solved simultaneously using the finite element method (FEM) in COMSOL Multiphysics 5.2a. For the current work, tetrahedral type unstructured meshes are used since they have the ability to perform element structuring for complex geometries and the domain does not have to undergo domain decomposition [41]. A segregated solver is used because it can balance memory requirements and solution accuracy simultaneously. First order discretisation is used together with quadratic elements for the temperature field. Second order discretisation is only suitable for creeping flows which will not be exploited in this work since viscous flow study is not considered. The relative error tolerance is set at 0.001 and a grid independence test (GIT) is performed to identify a suitable mesh to get an accurate output with the shortest simulation running time. Different numbers of elements (76316, 196887, 386092, 1034900 and 3276705) were used, as shown in **Fig. 2**. On the basis of these results, the mesh with 1034900 elements is considered a suitable compromise between accuracy and computational cost. It has significant mesh refinement at the base of the channel and at the contact region between the fluid and the solid areas to resolve the boundary layer accurately.

The present model was compared to previous numerical and experimental studies. The first study was an experimental investigation of a straight micro-channel MCHS conducted by

Kawano et al. [42]. The second validation was against the numerical study presented by Qu and Mudawar [43]. Both studies, used the same material (silicon) and dimensions of the micro-channel were 180μm, 57μm, 10mm the height, width and length, respectively. The top of the micro-channel was subjected to a uniform heat flux of $90W/cm^2$, while the side walls of the micro-channel were set to be symmetric in terms of heat transfer, with an adiabatic boundary condition at the bottom wall. Laminar flow was utilized in the studies with Re ranging from 80 to 400. **Fig. 3** shows that the present numerical method agrees very well with the previous experimental and numerical studies.

5. Results and discussion

In this study, the effect of different parameters has been studied under laminar flow conditions (Re ranging from 100 to 2300) using the CFD model. The parameters cover a wide range of radii, sizes and positions of the VGs to explore their effect on the conjugate heat transfer. The VGs are semi-circular cylinders with length, $W_2 = 350\mu m$ (see **Fig. 1**) and a constant heat flux relevant to micro-chips water cooling applications is applied at the bottom of the micro-channel $100Wcm^{-2}$ [27].

5.1 θ and the temperature distribution analysis

θ decreases with increasing velocity of the liquid phase (increasing Re) since heat is transferred away at a higher rate for larger velocities. There is however an unwanted increase in ΔP as velocity increases.

5.1.1 Effect of varying the radius of VGs on θ

From **Fig. 4,** for uniform channels and all channels with VGs at all values of Re, θ decreases monotonically as Re increases since at higher velocity the rate of heat transfer increases.

This is because at low Reynolds number, the inertia of liquid flow moving over the VGs does not provide sufficiently large vortices to transfer the heat from the hot region to the cold region of the water. Instead, the fluid immediately behind the VGs is essentially stagnant, resulting in local hotspots and the associated increase in thermal resistance. More generally at low Re, there is much less intermixing between hot and cold fluid regions. Of key influence on the level of intermixing is that, at higher Re, the VGs will generate increasingly larger vortices which break the hydrodynamic and thermal boundary layers, as shown in **Fig. 5**. Interestingly, **Fig. 5** also shows two types of vortices which are transverse and longitudinal, which combine increasingly to enhance the heat transfer as Re is increased. However, the pressure penalty is also increased.

From **Fig. 4**, it is seen that the reduction in θ at high Re is consistent, for a range of VG radii, at all Re.

Referring to **Fig. 4**, it shows clearly that θ decreases as the radii of the VGs are increased. This is due to more effective breakage of the thermal boundary layer improving heat transfer when using a large radius of 300 μm, whereas the highest θ is for the uniform channel. Furthermore, **Fig. 6** explains the reduction in θ when increasing the radius, for instance, at R = 300μm, results from increased liquid mixing – this is shown by the contrast between the blue (hot liquid) and red (cold liquid) particles (see **Fig. 6(C)**). This observation is further clarified by the velocity contours and arrow surface plot from **Fig. 6**. It shows how the recirculation region expands as the VGs' radii are increased (see the enlarged image of red dashed box in **Fig. 6**) improving the heat transfer as the boundary layer is broken up. Furthermore, as the radius increases the velocity contour above the VGs indicates higher liquid velocities are induced. Higher liquid velocity results in increased rate of heat transfer as more liquid passes through the channel compared with low liquid velocity. The temperature distribution for various VG radii are shown in **Fig. 7** as the temperature distribution is consistent with the plot of **Fig. 4** where θ decreases when the radius is increased. The average percentage θ improvement for R at 100μm, 200μm and 300μm are 3.06%, 3.85% and 5.46% respectively which corresponds to **Fig. 4**. From **Fig. 6**, at increasing radius of 100μm, 200μm and 300μm, the velocity contours change significantly between the moving fluids and the static fluid. The same behaviour occurs for the VGs placed at the middle and back positions. In fact, the increase in radius results in higher ΔP due to more restricted flow through the narrow channel; this is discussed in detail in **section 5.2**.

5.1.2 Effect of varying the distance between VGs on θ

The temperature distributions at the y-z and y-x cross sections are presented in **Fig. 8**. The cross-section is just upstream of the last rib. This demonstrates the temperature distribution and flow structure after fluid vortices have hit the earlier VGs, indicating the effectiveness of the proposed variables to remove heat from the system. It can be observed that the temperature of the substrate increased when the distance between VGs D = 100μm, but that increasing D for D ≥ 100μm, has only a minimal effect. The lowest temperature can be achieved when the VGs are adjacent to one another. The same trend occurs when VGs are placed at the middle or the back of the MCHS. The reason behind this behaviour is explained by using a particle tracing method, shown in **Fig. 9**, where the blue particles which are moving in between the gap of the VGs and the MCHS wall are displaced to the positive y-direction of the MCHS after going through all the 5 VGs.

This behaviour improves heat transfer as it covers most of the bottom surface area of the MCHS and carries more heat away from it. In addition, the red particles moving over the VGs meet the blue particles downstream of the last rib, as can be seen clearly in **Fig. 9 (B)**. The mixing of blue and red particles improves the heat transfer and at D = 0μm this effect is greatest. With larger distances between the VGs, the fluid behaviour is more predictable and less fluid mixing occurs where the fluid is almost moving in a straight path. Furthermore, the observation from the particle tracing analysis is clarified by the addition of arrow surfaces created in **Fig. 8 (A)** and **Fig. 8 (B)**. At D = 0μm, it is observed that the recirculation regions occur near the bottom of the MCHS (anti-clockwise) and at the upper part of the fluid region (clockwise). The opposing directions of the recirculation regions enhances the mixing of the hot and cold fluid regions. The hot fluid from the bottom of the MCHS recirculates upwards towards the centre of the channel while the upper part recirculation region brings the recirculated hot fluid from sidewalls. This mixing breaks the boundary layer at both the bottom and sidewalls of the channel.

The temperature plot in **Fig. 8** agrees with the θ plot in **Fig. 10**. From **Fig. 10**, the trend is similar for all cases. At distances of 100μm, 200μm and 300μm the plot almost overlaps with the uniform channel (R = 0μm) plot indicating the conjugate heat transfer improvement is not significant with higher distances between the VGs. On the other hand, the plot at D = 0μm shows more significant improvements in θ improvement in **Fig. 10**, represented by the red line. The red plot does not overlap with the other plots and has the lowest θ at every Re which agrees with the temperature plot in **Fig. 8 (A)**. The average percentage θ improvement for D values at 0 μm, 100μm, 200μm and 300μm compared to uniform channel are 3.06%, 1.97%, 2.11% and 2.10% respectively which corresponds to **Fig. 10** which agrees with temperature distribution in **Fig. 8**.

5.1.3 Effect of VG positioning on θ

The same procedure was carried out for the other 2 VG locations at the middle and back and similar conclusions were drawn: in **Fig. 10** the lowest θ is at D = 0μm for the reasons discussed in relation to **Fig. 9**. A comparison between the lowest θ values trend at each position is however carried out in **Fig. 11** where the lowest θ is achieved at the front position but there are insignificant differences between the plots. VGs at the front position have the lowest θ compared to the other two positions. Using the same cross-section utilised by **Fig. 8**, referring to **Fig. 12**, the temperature contours (left side plot) from three positions show that the front position has the lowest temperature magnitude while the back position has the highest, which agrees with the θ plot in **Fig. 11**. From the z-direction velocity contour plot in **Fig. 12** (right side plot), as the vortices formed from the three positions of the VGs it can be seen that the front position (**Fig. 12 (A)**) creates the highest downwards velocity magnitude near the sidewalls of the microchannel indicating more heat is being carried away from the sidewalls. The average percentageimprovement in θ for the front, middle and back cases are 3.06%, 2.75% and 2.98% respectively which corresponds to **Fig. 11**. Based in **Fig. 11**, the position of the VGs does not have a significant effect on the conjugate heat transfer in the system. The different positions of the VGs also affect the ΔP and this will be discussed thoroughly in the next part of the study.

5.2 ΔP analysis

ΔP, the pressure difference between the inlet and outlet of the MCHS, is another important parameter. It should be reduced to a minimum in order to minimize the hydraulic power input required to generate the flow.

5.2.1 Effect of varying the radius of VGs on ΔP

The effect of varying the radius between 0μm to 300μm is investigated first. **Fig. 13** shows how ΔP increases when the radius increases and that this effect becomes more pronounced as Re is increased too. This is due to increased constriction of the flow at larger radii which leads to larger localised flow velocities and increased separation behind the VGs. The former effect in particular is shown in **Fig. 14**. The average percentage increase of ΔP for R values of 100μm, 200μm and 300μm are 3.91%, 14.27% and 40.04% respectively which corresponds to **Fig. 13,** indicating that very large pressure drops are induced compared to the enhancement of thermal resistance in **section 5.1.1**.

5.2.2 Effect of varying the distance between VGs on ΔP

The effect of the distance between the VGs is investigated for the constant radius of 100μm. The distance is varied from 0μm to 300μm in each case. **Fig. 15** shows that generally the pressure is slightly higher than for the uniform channel, but that the influence is small since no turbulence is generated. The lowest ΔP is achieved at D = 100μm at every position, while the highest ΔP is when the distance between VGs is 0μm. At distances of 200μm and 300μm, the pressure increases lie between these two extremes, with that for 300μm higher than for 200μm. The highest ΔP at 0μm separation distance between VGs, is due to the channel having a converging/diverging profile which acts like a nozzle increasing the local flow velocities near the VGs. The higher *ΔP* with D = 0μm can also be explained by **Fig. 8 (A)** where vigorous mixing between recirculation regions is evident, providing increased flow resistance in the stream-wise direction. The lowest pressure difference at D = 100μm is due to the greater flow uniformity compared to other distances, **Fig. 9**. **Fig. 15**, shows the results for high Re since these are the most significant ones in terms of *ΔP*. The average percentage increase of *ΔP* for D values of 0μm, 100μm, 200μm and 300μm are 4.40%, 2.31%, 2.58% and 3.14% respectively, which agrees with **Fig. 15**.

5.2.3 Effect of VGs positioning on *ΔP*

Since the distance between VGs is not very influential the case with D = 0μm is chosen to study the influence of the front, middle and back position on the *ΔP* of the system. **Fig. 16** compares the *ΔP* for different positions of the VGs. It is found that the largest *ΔP* is at the front position, while the lowest is at the back position due to the higher intensity of downwards velocity of fluid near the sidewalls of the channel. The average percentage *ΔP* increase for front, middle and back position are 2.70%, 2.53% and 2.32% respectively which are very close to each other (refer to **Fig. 16** for the graph).

5.3 Thermal-hydraulic performance index analysis

To measure the overall performance of the heat sink, in terms of the balance between θ and *ΔP*, the parameters of θ and *ΔP* are combined in equation (8). Values of PEC > 1 means the overall performance of a modified micro-channel is better than the uniform conventional channel. From **Fig. 17**, the highest PEC region occurred for a radius of 100μm whereas the PEC indices at 300μm are much lower than for minor rib radii. This is because the minor improvements in θ are dominated by the corresponding large increase in *ΔP*. The highest PEC occurred at the radius of 100μm and the distance between VGs of 0μm for the front position of the VGs. Referring to **Fig. 17**, the highest PEC index occurred at R = 100μm and D = 0μm. Only at R = 100μm does the PEC exceeds unity which means its overall performance is better than the uniform conventional channel. Every position shows the highest PEC index at R=100μm and D=0μm. **Fig. 18** compares the effect of VG position for R=100μm and D=0μm.

The effects of the VG distance on the PEC index is carried out for Re = 900. The distance between VGs is varied from 0μm to 500μm at every position. **Fig. 19** shows that the PEC index increases as the distance between VGs decreases, at D=0μm, the PEC index is the highest for all cases, however, the front position is found to be the highest. The high PEC index is due to

ΔP decreasing at a faster rate than θ. Thus, it can be concluded that increasing the distance between VGs is not beneficial for the overall performance of the micro-channel.

The above results show that the best combination is to use VGs at the front position with 0µm distance between them. Finally, with this combination, the effect of changing the radius of the VGs (from 0µm to 300µm) on the PEC index is shown in **Fig. 20**. The PEC index decreases gradually for R>150µm and it increases at the radius below 150µm. The results show that the highest PEC index is found at the radius of 100µm. This is the best compromise between improving thermal performance and mitigating the inevitable rise in ΔP. From all PEC plots, it can be seen that the PEC values do not show a significant increase when calculated against the smooth channel since the thermal resistance reduction is dominated by large pressure drop increase which is similar to the findings of Liu et al. [34, 38]

6. Conclusion

This study explores the enhancement in conjugate heat transfer that can be achieved using cylindrical vortex generators (VGs). A group of five VGs is applied at the base of a uniform micro-channel heat sink (MCHS) using three positions (front, middle and back). The influence of the VGs' radii in the range of (0-300) µm and the distance between the VGs (0-300) µm across a water-filled micro-channel are also investigated by COMSOL Multiphysics® software. The geometries are assessed for Re in the range of 100 to 2300 using thermal resistance (θ), pressure drop (ΔP) and a thermal hydraulic performance index (PEC) which combines both of θ and ΔP. The performance of VGs is evaluated with reference to the uniform micro-channel (without VGs). The main findings are as follows.

- It was found that using cylindrical VGs enhances the thermal performance of the MCHS but incurs a high pressure penalty. The cylindrical VGs promote vortices which improve the heat transfer by fluid mixing which is visualised effectively using three-dimensional tracer particle-trajectory plots. It is also found that the θ decreases (the heat transfer performance is enhanced) with an increase of the VGs' radii. The results showed that the best heat transfer enhancement is achieved at front position using radii of 300 µm and no distance between the VGs (D=0 µm).
- The influence of the distance between VGs was also investigated, and it was shown that a short distance (e.g. 100 µm) between the VGs improves θ more effectively compared to larger distances (e.g. 500 µm).

- The effect of the position of the VGs was also considered. It was found that the front position is the best for enhancing the heat transfer and the pressure penalty was reduced very slightly when moving the VGs to the back of the channel.
- The thermal hydraulic performance (PEC) was investigated by measuring the overall performance of the micro-channel accounting for the combination of the θ and ΔP terms. Interestingly, it is not necessarily the lowest thermal resistance that gives the highest PEC index, for instance, the lowest θ at R=300 µm and Re of 2300, but in terms of PEC, the radius of 100µm has its highest value at Re=900.
- From the PEC index perspective, results demonstrate that the PEC index is an effective means of showing that increasing the radius is not beneficial due to the higher rate of pressure increase compared to the reduction in θ. This means that longer distances resulted in a reduction in the performance of the PEC index to values < 1..

Acknowledgement

We thank Basra Oil Company (BOC) and the Ministry of Oil, Iraq for their support to Mushtaq T. K. Al-Asadi.

7. References

[1] F. S. Alkasmoul, M. T. Al-Asadi, T. G. Myers, H. M. Thompson, and M. C. T. Wilson, "A practical evaluation of the performance of Al2O3-water, TiO2-water and CuO-water nanofluids for convective cooling," *International Journal of Heat and Mass Transfer,* vol. 126, Part A, pp. 639-651, 11// 2018.

[2] D. B. Tuckerman and R. F. W. Pease, "High-performance heat sinking for VLSI," *Electron Device Letters, IEEE,* vol. 2, no. 5, pp. 126-129, 1981.

[3] D. Yang, Y. Wang, G. Ding, Z. Jin, J. Zhao, and G. Wang, "Numerical and experimental analysis of cooling performance of single-phase array microchannel heat sinks with different pin-fin configurations," *Applied Thermal Engineering,* vol. 112, pp. 1547-1556, 2017/02/05/ 2017.

[4] I. A. Ghani, N. Kamaruzaman, and N. A. C. Sidik, "Heat transfer augmentation in a microchannel heat sink with sinusoidal cavities and rectangular ribs," *International Journal of Heat and Mass Transfer,* vol. 108, pp. 1969-1981, 2017/05/01/ 2017.

[5] W. A.-S. Amer Al-Damook, Mushtaq T. Al-Asadi, Nabeel Abed, Wissam H. Khalil, "Hydrothermal Performance Enhancement in Different Types of Perforated Heat Sinks: a Review," *Journal of Multidisciplinary Engineering Science and Technology (JMEST),* review vol. 5, no. 10, October - 2018.

[6] M. T. Al-Asadi, H. A. Mohammed, S. N. Akhtar, A. S. Kherbeet, and H. K. Dawood, "Heat Transfer Enhancements Using Traditional Fluids and Nanofluids in Pipes with Different Orientations: A Review," *Journal of Nanofluids,* vol. 6, no. 6, pp. 987-1007, // 2017.

[7] M. T. Al-asadi, H. A. Mohammed, A. S. Kherbeet, and A. A. Al-aswadi, "Numerical study of assisting and opposing mixed convective nanofluid flows in an inclined circular pipe," *International Communications in Heat and Mass Transfer,* vol. 85, pp. 81-91, 7// 2017.

[8] M. T. Al-Asadi, Al-Sallami W. T. , "Do ionic liquids replace water or nanofluids to enhance heat transfer in micro-channel systems?," presented at the XI International Conference on Computational Heat and Mass Transfer, Cracow, Poland, 21-24 May 2018

[9] A. S. Kherbeet *et al.*, "Mixed convection nanofluid flow over microscale forward-facing step — Effect of inclination and step heights," *International Communications in Heat and Mass Transfer,* vol. 78, pp. 145-154, 11/ 2016.

[10] J. Albadr, S. Tayal, and M. Alasadi, "Heat transfer through heat exchanger using Al2O3 nanofluid at different concentrations," *Case Studies in Thermal Engineering,* vol. 1, no. 1, pp. 38-44, 10/1/ 2013.

[11] M. T. Al-Asadi, "Evaluation of nanofluids performance with vortex generators for enhanced micro-channel heat transfer," in *ICTEA: International Conference on Thermal Engineering*, 2018, vol. 2018.

[12] A. S. Kherbeet *et al.*, "Heat transfer and fluid flow over microscale backward and forward facing step: A review," *International Communications in Heat and Mass Transfer,* vol. 76, pp. 237-244, 8// 2016.

[13] C. Huang, W. Cai, Y. Wang, Y. Liu, Q. Li, and B. Li, "Review on the characteristics of flow and heat transfer in printed circuit heat exchangers," *Applied Thermal Engineering,* vol. 153, pp. 190-205, 2019/05/05/ 2019.

[14] T. Ambreen, A. Saleem, and C. W. Park, "Pin-fin shape-dependent heat transfer and fluid flow characteristics of water- and nanofluid-cooled micropin-fin heat sinks: Square, circular and triangular fin cross-sections," *Applied Thermal Engineering,* vol. 158, p. 113781, 2019/07/25/ 2019.

[15] T. Johnson and P. Joubert, "The influence of vortex generators on the drag and heat transfer from a circular cylinder normal to an airstream," *Journal of Heat Transfer,* vol. 91, no. 1, pp. 91-99, 1969.

[16] J. M. Wu and W. Q. Tao, "Numerical study on laminar convection heat transfer in a rectangular channel with longitudinal vortex generator. Part A: Verification of field synergy principle," *International Journal of Heat and Mass Transfer,* vol. 51, no. 5–6, pp. 1179-1191, 3/ 2008.

[17] C. Liu *et al.*, "Experimental investigations on liquid flow and heat transfer in rectangular microchannel with longitudinal vortex generators," *International Journal of Heat and Mass Transfer,* vol. 54, no. 13, pp. 3069-3080, 2011/06/01/ 2011.

[18] A. Ebrahimi, E. Roohi, and S. Kheradmand, "Numerical study of liquid flow and heat transfer in rectangular microchannel with longitudinal vortex generators," *Applied Thermal Engineering,* vol. 78, pp. 576-583, 2015.

[19] C. Chen *et al.*, "A study on fluid flow and heat transfer in rectangular microchannels with various longitudinal vortex generators," *International Journal of Heat and Mass Transfer,* vol. 69, pp. 203-214, 2014/02/01/ 2014.

[20] A. Ebrahimi, F. Rikhtegar, A. Sabaghan, and E. Roohi, "Heat transfer and entropy generation in a microchannel with longitudinal vortex generators using nanofluids," *Energy,* vol. 101, pp. 190-201, 4/15/ 2016.

[21] G. Lu and X. Zhai, "Analysis on heat transfer and pressure drop of a microchannel heat sink with dimples and vortex generators," *International Journal of Thermal Sciences,* vol. 145, p. 105986, 2019/11/01/ 2019.

[22] Y. J. Cheng, "Numerical simulation of stacked microchannel heat sink with mixing-enhanced passive structure," *International Communications in Heat and Mass Transfer,* vol. 34, no. 3, pp. 295-303, 2007/03/01/ 2007.

[23] M. T. Al-Asadi, F. S. Alkasmoul, and M. C. T. Wilson, "Benefits of spanwise gaps in cylindrical vortex generators for conjugate heat transfer enhancement in micro-channels," *Applied Thermal Engineering,* 2017.

[24] A. Datta, D. Sanyal, and A. K. Das, "Numerical investigation of heat transfer in microchannel using inclined longitudinal vortex generator," *Applied Thermal Engineering,* vol. 108, pp. 1008-1019, 2016.

[25] C.-C. Wang, J. Lo, Y.-T. Lin, and M.-S. Liu, "Flow visualization of wave-type vortex generators having inline fin-tube arrangement," *International Journal of Heat and Mass Transfer,* vol. 45, no. 9, pp. 1933-1944, 4/ 2002.

[26] M. T. Al-Asadi, A. Al-damook, and M. C. T. Wilson, "Assessment of vortex generator shapes and pin fin perforations for enhancing water-based heat sink performance," *International Communications in Heat and Mass Transfer,* vol. 91, pp. 1-10, 2// 2018.

[27] M. T. Al-Asadi, F. S. Alkasmoul, and M. C. T. Wilson, "Heat transfer enhancement in a micro-channel cooling system using cylindrical vortex generators," *International Communications in Heat and Mass Transfer,* vol. 74, pp. 40-47, 5/ 2016.

[28] C. Min, C. Qi, X. Kong, and J. Dong, "Experimental study of rectangular channel with modified rectangular longitudinal vortex generators," *International Journal of Heat and Mass Transfer,* vol. 53, no. 15–16, pp. 3023-3029, 7/ 2010.

[29] E. Hosseinirad, M. Khoshvaght-Aliabadi, and F. Hormozi, "Evaluation of heat transfer and pressure drop in a mini-channel using transverse rectangular vortex-generators with various non-uniform heights," *Applied Thermal Engineering,* vol. 161, p. 114196, 2019/10/01/ 2019.

[30] K.-C. Wong and J.-H. Lee, "Investigation of thermal performance of microchannel heat sink with triangular ribs in the transverse microchambers," *International Communications in Heat and Mass Transfer,* vol. 65, pp. 103-110, 2015/07/01/ 2015.

[31] M. Samadifar and D. Toghraie, "Numerical simulation of heat transfer enhancement in a plate-fin heat exchanger using a new type of vortex generators," *Applied Thermal Engineering,* vol. 133, pp. 671-681, 2018.

[32] M. Khoshvaght-Aliabadi, Z. Baneshi, and S. F. Khaligh, "Analysis on performance of nanofluid-cooled vortex-generator channels with variable longitudinal spacing among delta-winglets," *Applied Thermal Engineering,* vol. 122, pp. 1-10, 2017.

[33] G. Lu and X. Zhai, "Analysis on heat transfer and pressure drop of a microchannel heat sink with dimples and vortex generators," *International Journal of Thermal Sciences,* vol. 145, 2019.
[34] H.-Y. Li, W.-R. Liao, T.-Y. Li, and Y.-Z. Chang, "Enhancing heat transfer in a plate-fin heat sink using delta winglet vortex generators," *International Journal of Heat and Mass Transfer,* vol. 112, pp. 940-949, 2017.
[35] Y. F. Li, G. D. Xia, D. D. Ma, Y. T. Jia, and J. Wang, "Characteristics of laminar flow and heat transfer in microchannel heat sink with triangular cavities and rectangular ribs," *International Journal of Heat and Mass Transfer,* vol. 98, pp. 17-28, 2016/07/01/ 2016.
[36] M. Khoshvaght-Aliabadi, S. Zangouei, and F. Hormozi, "Performance of a plate-fin heat exchanger with vortex-generator channels: 3D-CFD simulation and experimental validation," *International Journal of Thermal Sciences,* vol. 88, pp. 180-192, 2015.
[37] L. Chai, G. D. Xia, and H. S. Wang, "Numerical study of laminar flow and heat transfer in microchannel heat sink with offset ribs on sidewalls," *Applied Thermal Engineering,* vol. 92, pp. 32-41, 2016/01/05/ 2016.
[38] H.-Y. Li, C.-L. Chen, S.-M. Chao, and G.-F. Liang, "Enhancing heat transfer in a plate-fin heat sink using delta winglet vortex generators," *International Journal of Heat and Mass Transfer,* vol. 67, pp. 666-677, 2013.
[39] *Comsol Multiphysics v.5.4, Heat Transfer Module User's Guide*. 2018.
[40] W. Qu and I. Mudawar, "Analysis of three-dimensional heat transfer in micro-channel heat sinks," *Int. J. Heat Mass Transfer,* vol. 45, pp. 3973 - 3985, 2002.
[41] J. Tu, G.-H. Yeoh, and C. Liu, *Computational Fluid Dynamics: A Practical Approach*. 2013.
[42] K. Kawano, K. Minakami, H. Iwasaki, and M. Ishizuka, "Micro channel heat exchanger for cooling electrical equipment," *ASME Heat Transfer Div Publ Htd,* vol. 361, pp. 173-180, 1998.
[43] W. Qu and I. Mudawar, "Analysis of three-dimensional heat transfer in micro-channel heat sinks," *International Journal of Heat and Mass Transfer,* vol. 45, no. 19, pp. 3973-3985, 09/01/ 2002.

Table captions

Table1: Dimensions of the MCHS. The variables R and D of the cylindrical VGs placed are also defined.

Table1: Dimensions of the MCHS. The variables R and D of the cylindrical VGs placed are also defined.

Parameters	Magnitude, µm
L	50000
H_1	900
H_2	700
W_1	250
W_2	175
W_3	150
R	0, 100, 200, 300
D	0, 100, 200, 300

Figure captions

Figure 1: **(A)** Full size of MCHS with the dimensions defined in Table 1. The geometrical representation of the MCHS, **(B)** The uniform channel without VGs, **(C)** The boundary conditions applied to the MCHS base**. (D)** MCHS having VGs placed at the bottom of the channel with the front view and side view and the interface surface between the liquid and solid.

Figure 2: Effect of mesh density on $\boldsymbol{\theta}$ and the ΔP.

Figure 3: Validation of the present work against experimental and Numerical work [42, 43].

Figure 4: Thermal resistance for different radii (100µm to 300µm) at the front position.

Figure 5: Water flow of VGs (R=400µm and the D=0µm) at the back of the channel; (A) Re=100, (B) Re=1900.

Figure 6: Particle tracing (red and blue streams) with the corresponding velocity (m/s) contours with a front arrangement (D=0 µm); (A) R=100µm, (B) R=200µm, (C) R=300µm.

Figure 7: Temperature contours (K) distribution (side-view) for various radii at the front position.

Figure 8: Temperature contours (K) with variable distances between VGs from 0 µm to 300 µm at Re=2300 for VGs in the front arrangement for y-z (front view) and y-z plane (top view).

Figure 9: Particle tracing; **(A)** for different distances ranging from of (0-500) µm at front position **(B)** zoomed in view at distance 0μm.

Figure 10: Thermal resistance against Re at difference distances between VGs (0µm, 100µm, 200µm and 300µm) at the front position.

Figure 11: Comparison of θ at the front, middle and back positions with the uniform channel case.

Figure 12: Temperature contours (K) (left side plot) and velocity contours (ms^{-1}) in z-direction (right side plot); (A) front (B) middle and (C) back.

Figure 13: Pressure drop against Re from 100 to 2300 and at the front position with the distance between VGs of 0μm.

Figure 14: The y-z cross section of the MCHS, with velocity contours (m/s) at different radii of 100μm, 200μm and 300μm at distance between VGs of 0μm for the front position.

Figure 15: Pressure drop against Re at every distance between VGs ranging from (0-300) μm for the front position at R = 100μm with zoomed in view.

Figure 16: Pressure drop for VGs placed at the front, middle and back with zoomed in view.

Figure 17: PEC index for different radii and distances between VGs of 0μm, 100μm, 200μm, and 300μm at the front position.

Figure 18: PEC index of different arrangements of VGs (front, middle and back) against Re with the boundary limit set to be 1 for a uniform channel.

Figure 19: PEC index plot against the distance between VGs at Re= 900 for 3 different positions.

Figure 20: PEC index for increasing radii at constant Re of 900 with distance, D = 0μm at the front position.

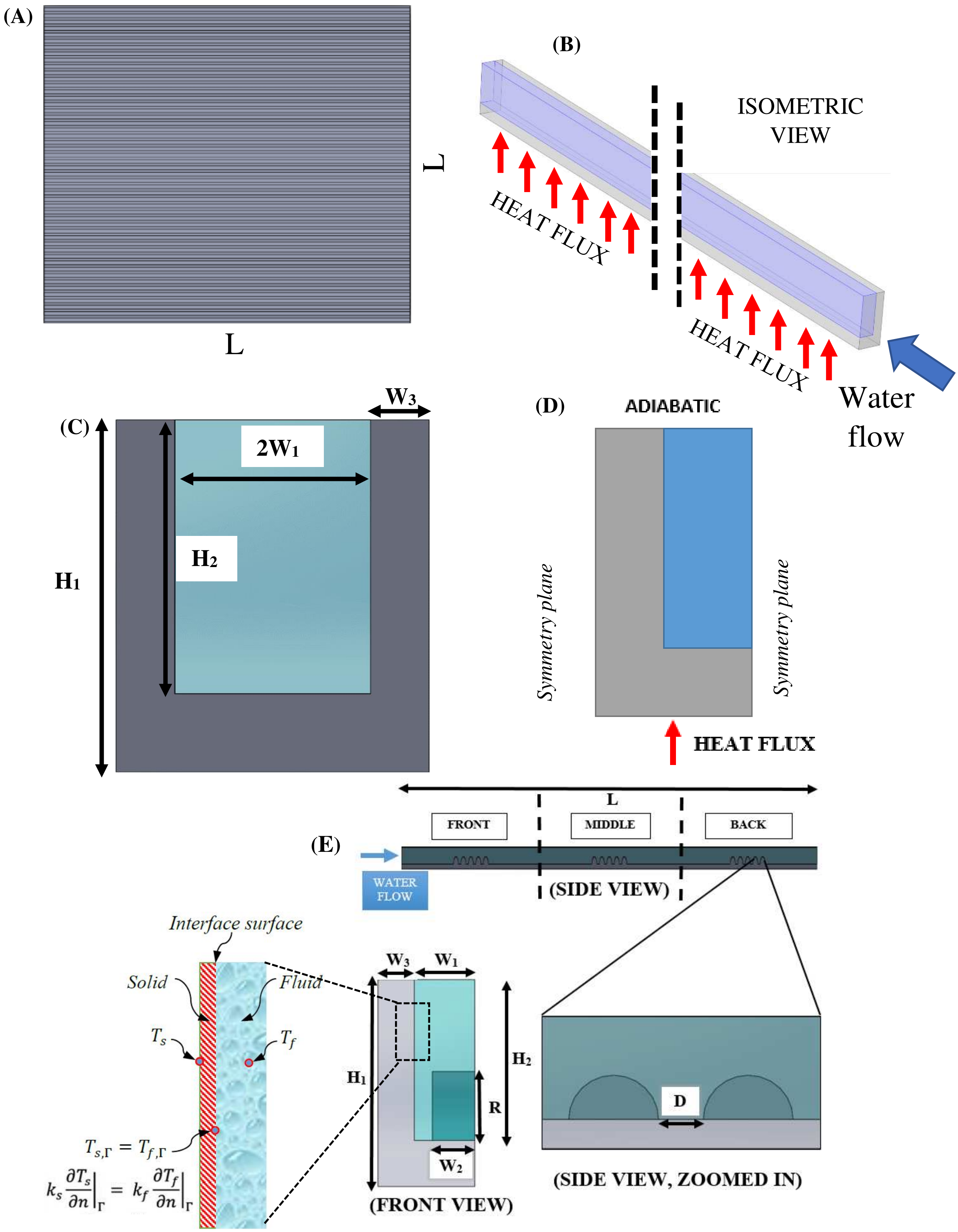

(A)
L
L
(B)
ISOMETRIC VIEW
HEAT FLUX
HEAT FLUX
Water flow
(C)
W_3
$2W_1$
H_2
H_1
(D)
ADIABATIC
Symmetry plane
Symmetry plane
HEAT FLUX
L
FRONT
MIDDLE
BACK
(E)
WATER FLOW
(SIDE VIEW)
Interface surface
Solid
Fluid
T_s
T_f
$T_{s,\Gamma} = T_{f,\Gamma}$
$k_s \frac{\partial T_s}{\partial n}\Big|_\Gamma = k_f \frac{\partial T_f}{\partial n}\Big|_\Gamma$
W_3
W_1
H_1
H_2
R
W_2
(FRONT VIEW)
D
(SIDE VIEW, ZOOMED IN)

Figure 1: **(A)** Full size of MCHS with the dimensions defined in Table 1. The geometrical representation of the MCHS, **(B)** The uniform channel without VGs, **(C)** The boundary conditions applied to the MCHS base**. (D)** MCHS having VGs placed at the bottom of the channel with the front view and side view and the interface surface between liquid and solid.

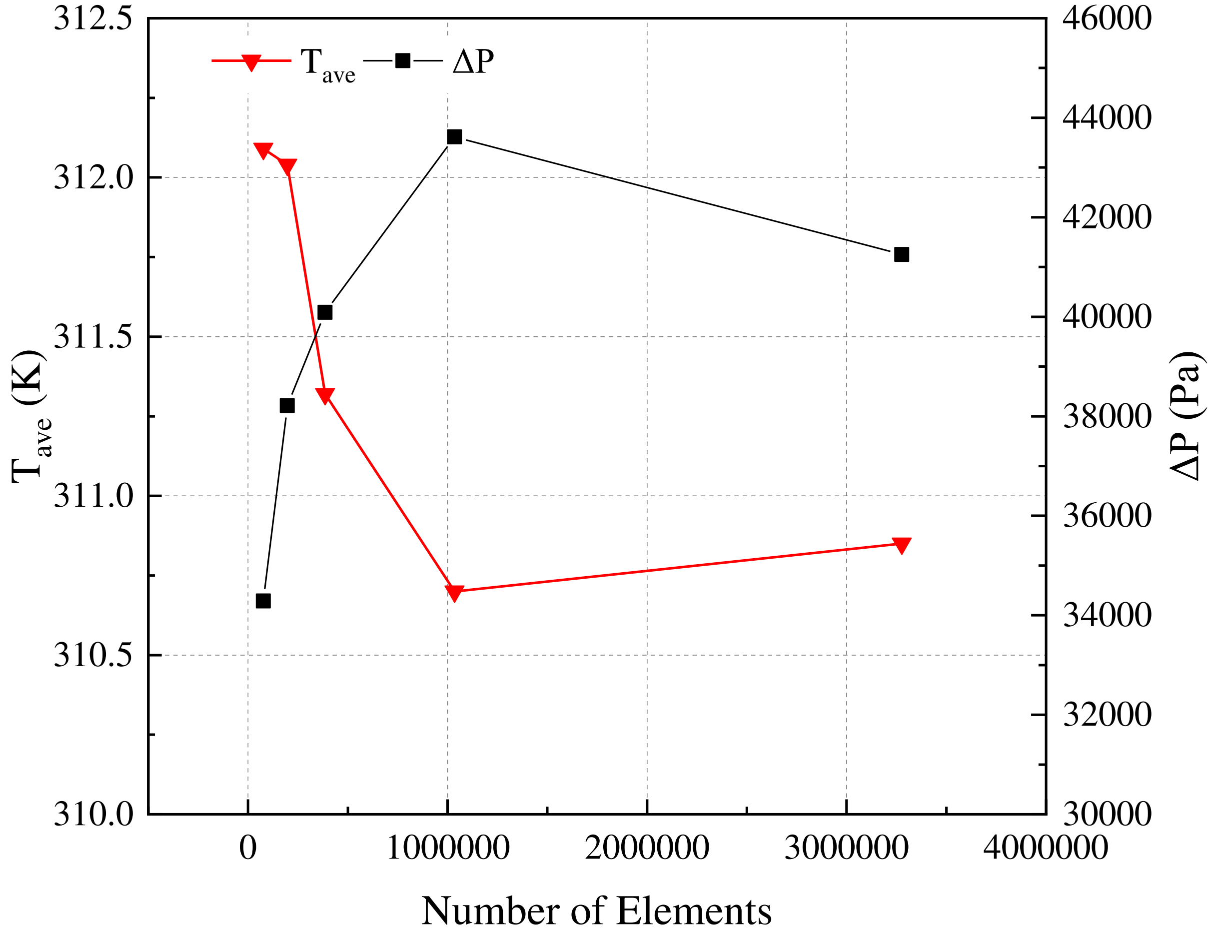

Figure 2: Effect of mesh density on θ and the ΔP.

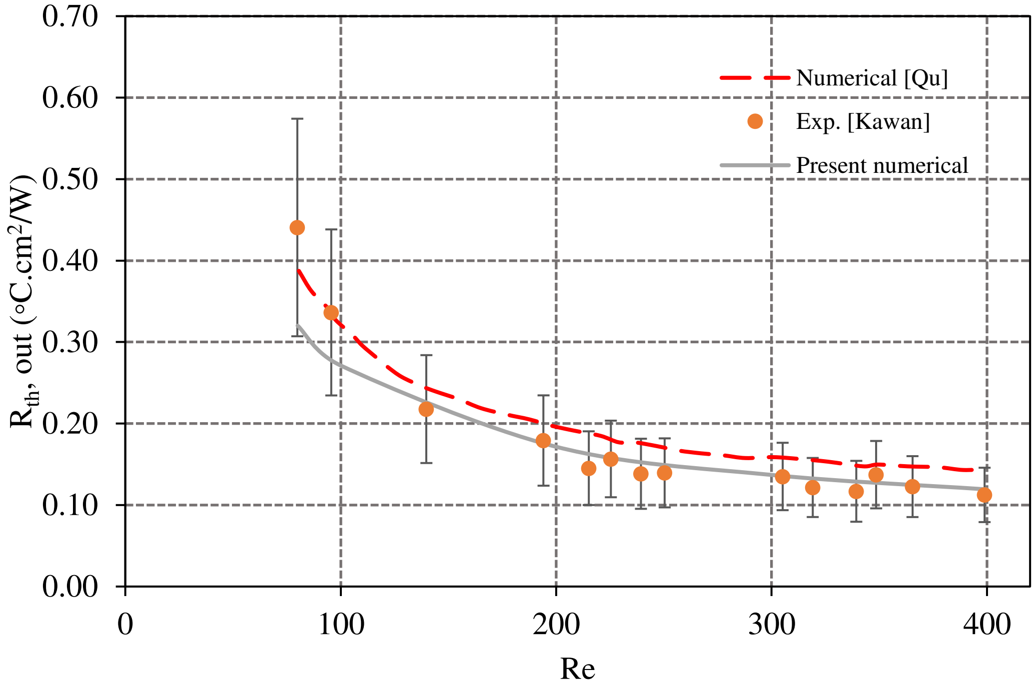

Figure 3: Validation of the present work against experimental and Numerical work [42, 43].

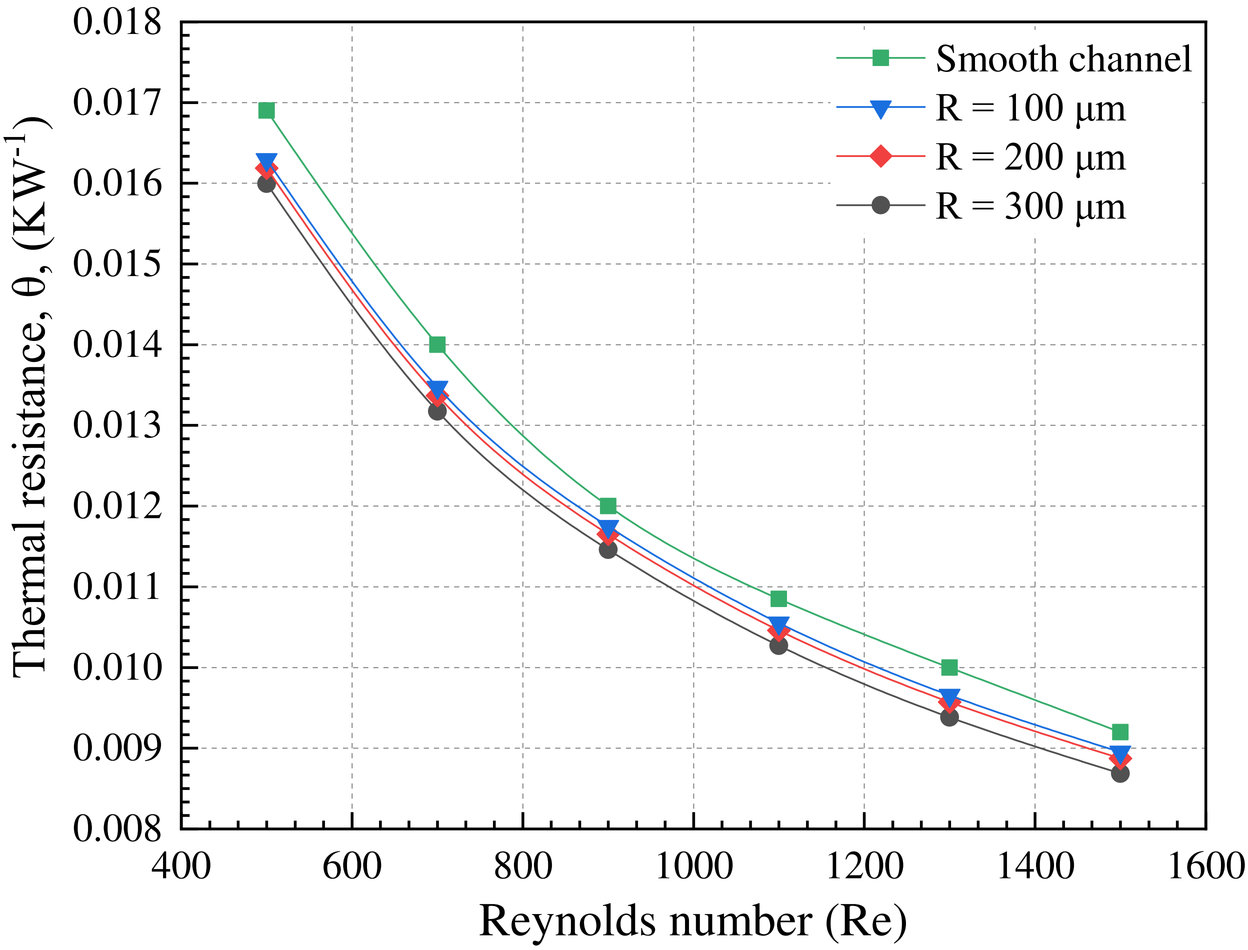

Figure 4: Thermal resistance for different radii (100µm to 300µm) at the front position.

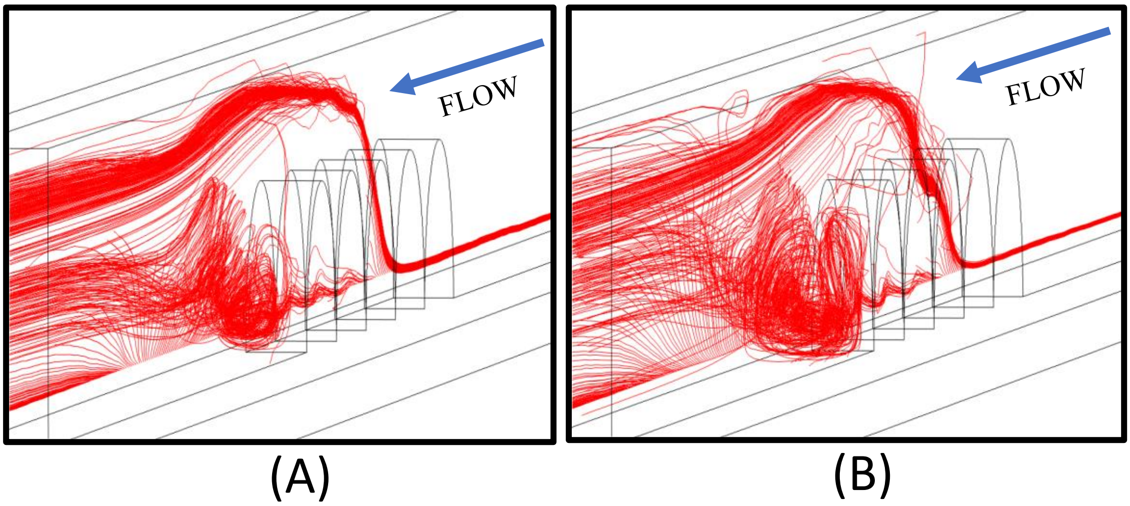

Figure 5: Water flow of VGs (R=400µm and the D=0µm) at the back of the channel; (A) Re=100, (B) Re=1900.

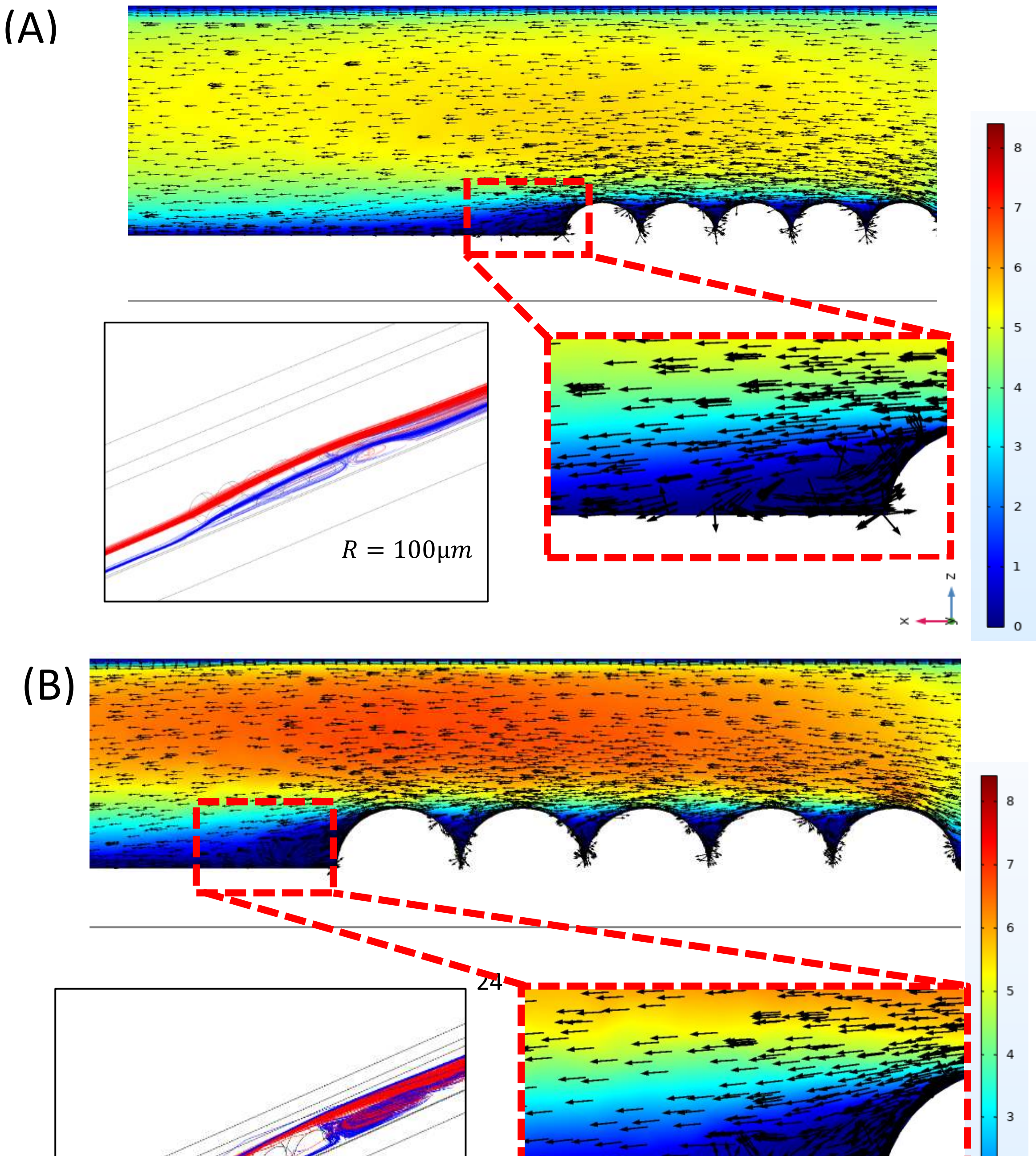

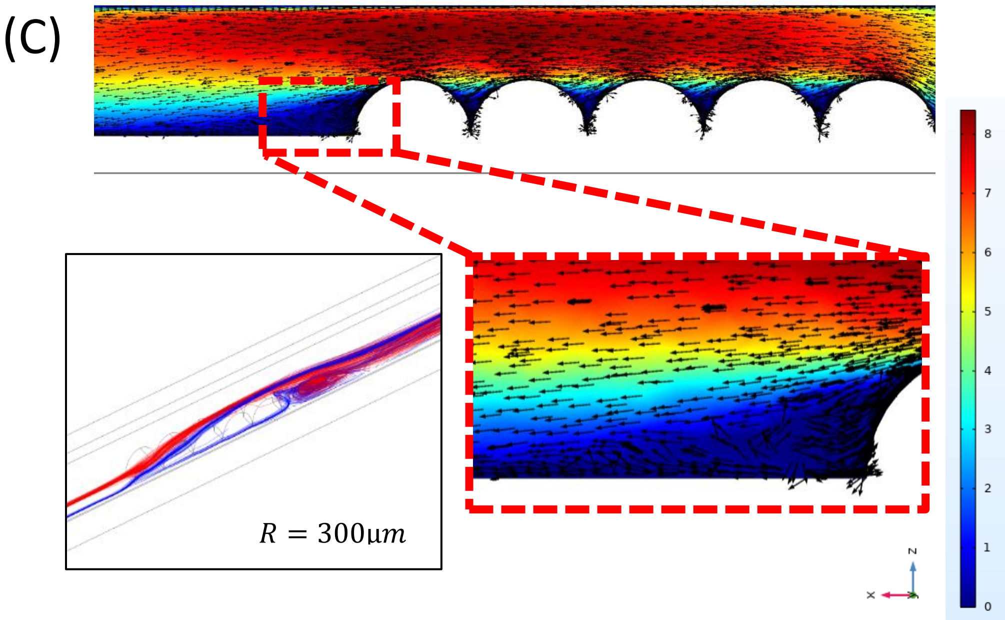

Figure 6: Particle tracing (red and blue streams) with the corresponding velocity (m/s) contours with a front arrangement (D=0 μm); (A) R=100μm, (B) R=200μm, (C) R=300μm.

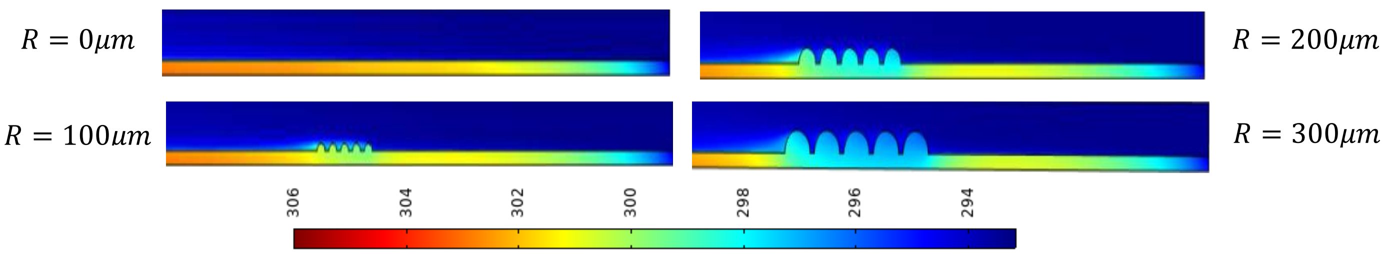

Figure 7: Temperature contours (K) distribution (side-view) for various radii at the front position.

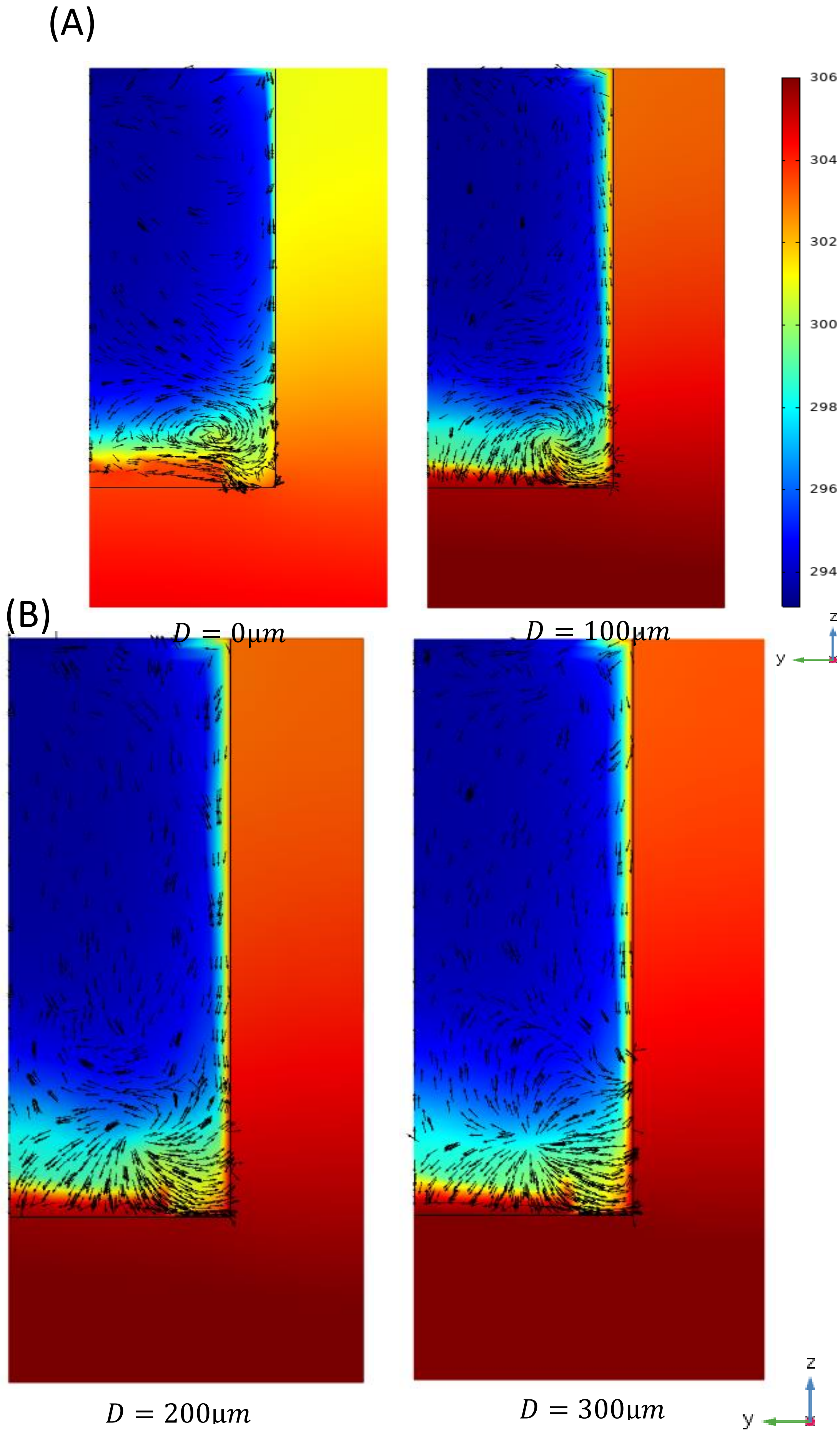
(A)
306
304
302
300
298
296
294
(B)
D = 0μm
D = 100μm
z
y
D = 200μm
D = 300μm
z
y

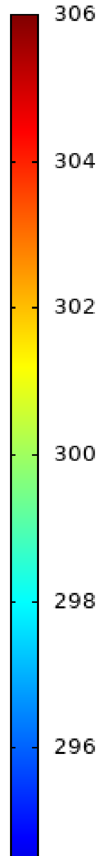
306
304
302
300
298
296

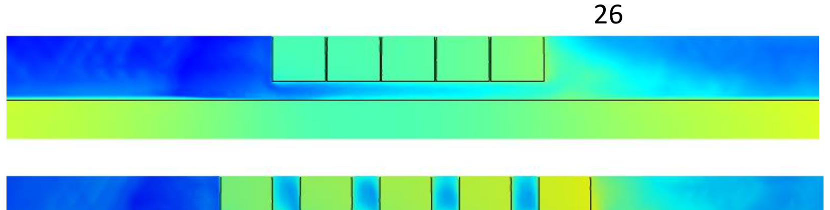

$D = 0\mu m$

Figure 8: Temperature contours (K) with variable distances between VGs from 0 µm to 300 µm at Re=2300 for VGs in the front arrangement for y-z (front view) and y-z plane (top view).

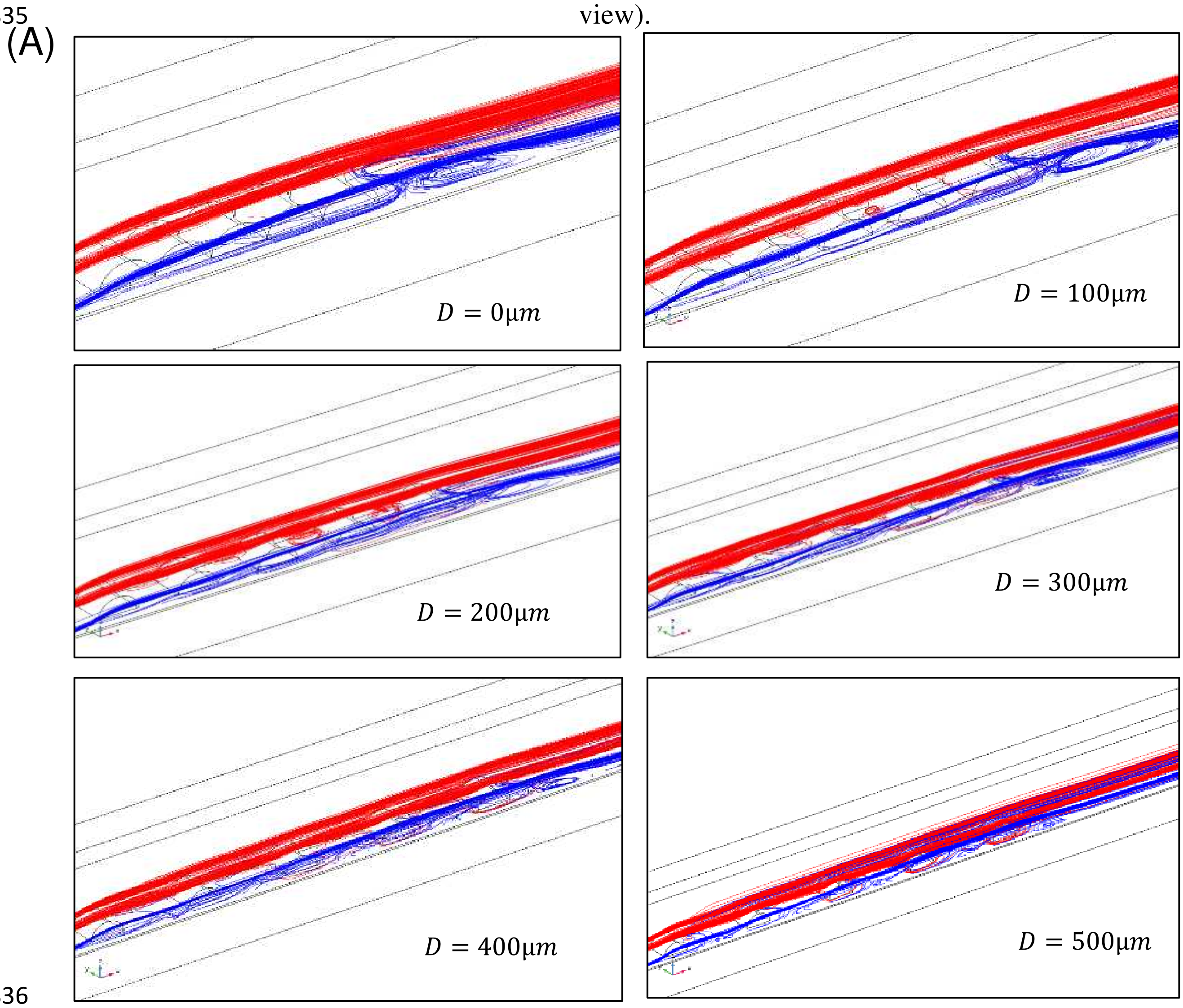

(B)

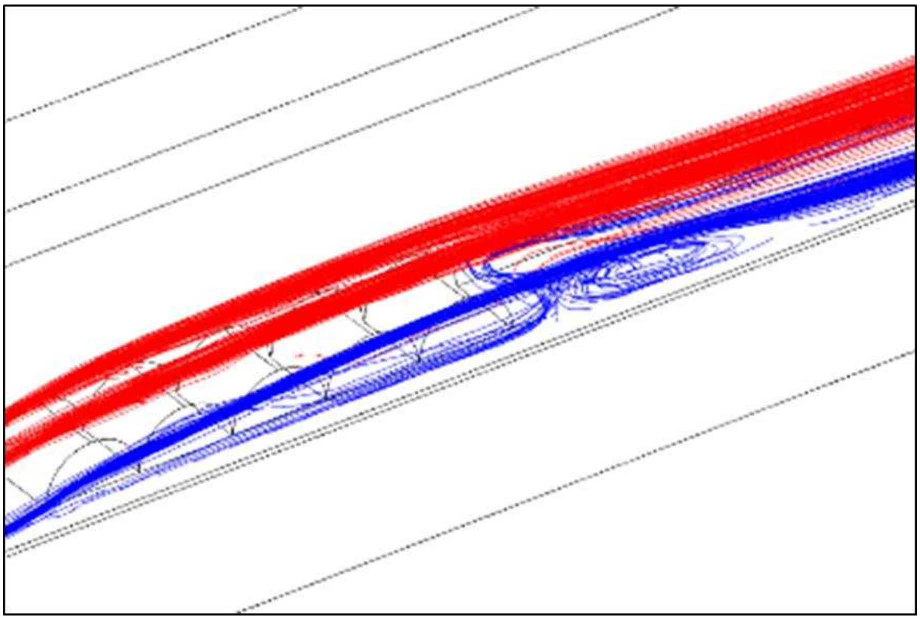

Figure 9: Particle tracing; **(A)** for different distances ranging from of (0-500) µm at front position **(B)** zoomed in view at distance 0μm.

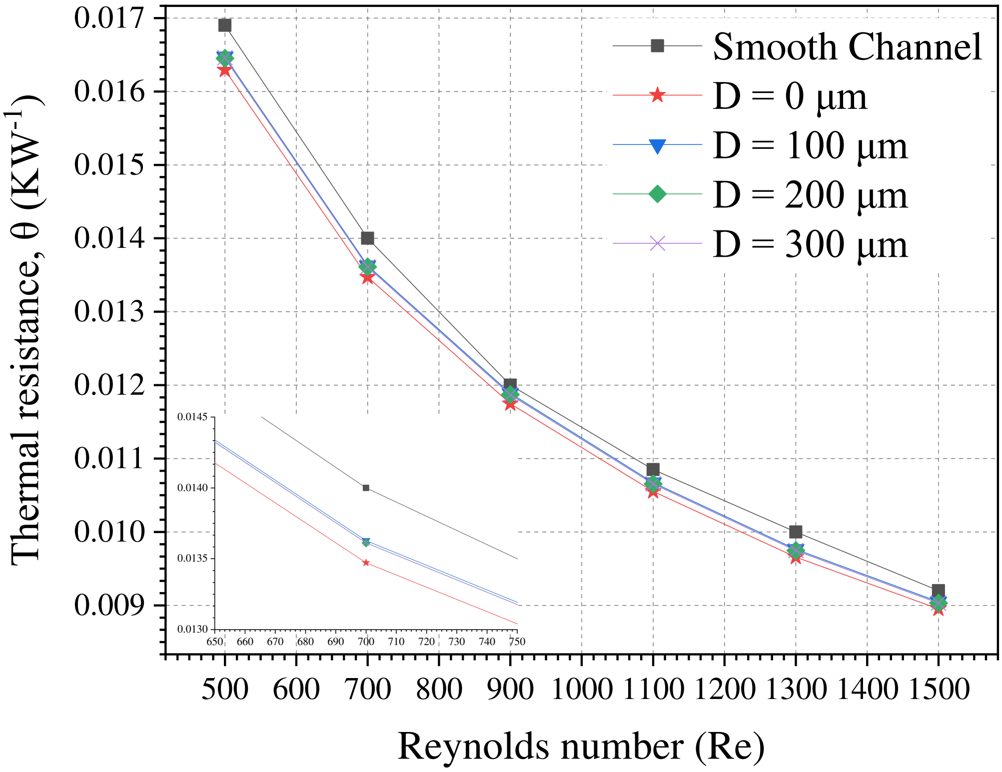

Figure 10: Thermal resistance against Re at difference distances between VGs (0µm, 100µm, 200µm and 300µm) at the front position.

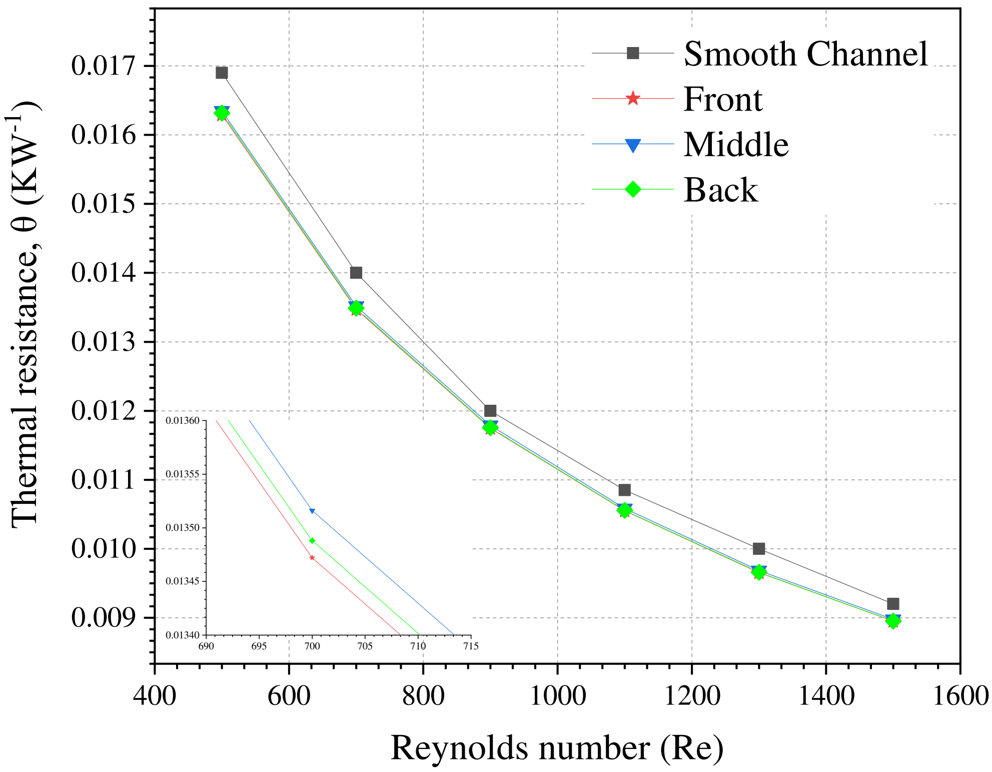

Figure 11: Comparison of θ at the front, middle and back positions with the uniform channel case.

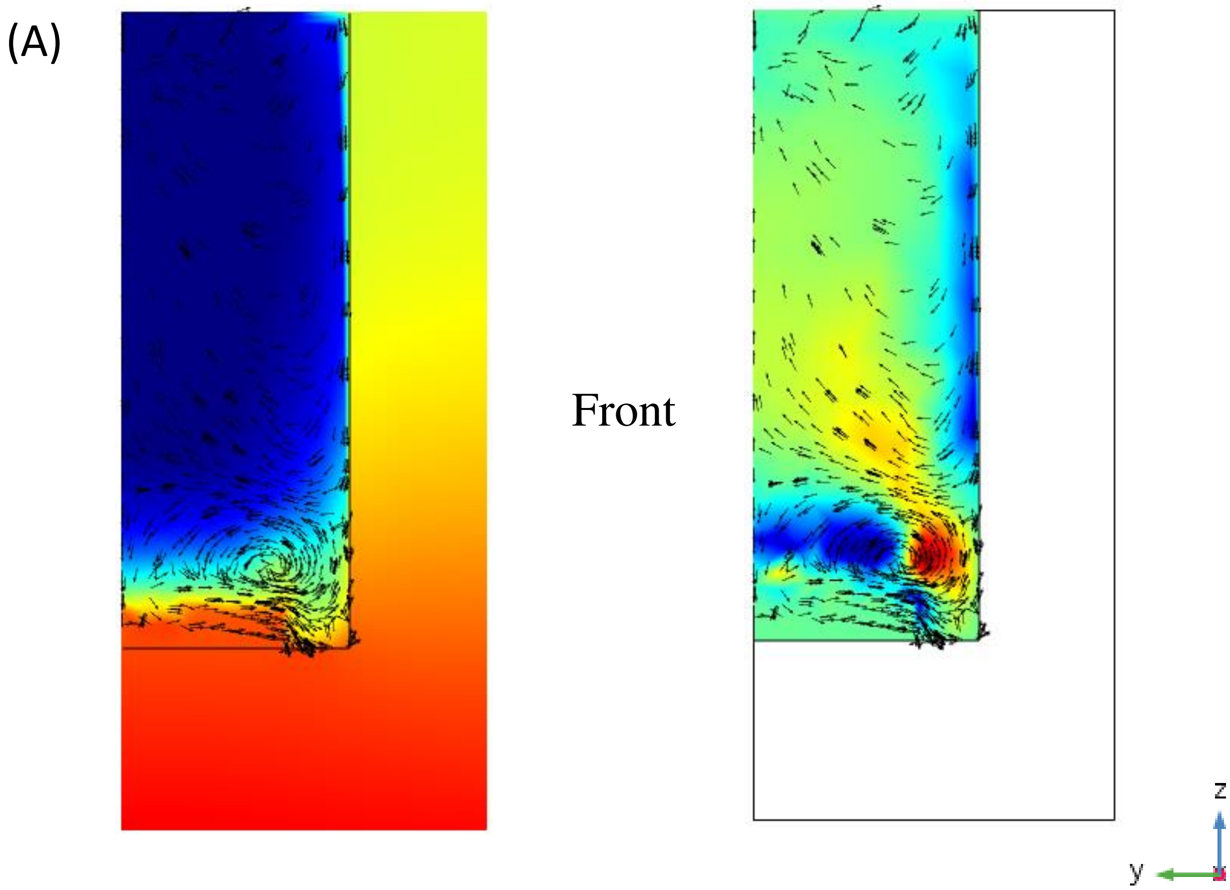

(B)

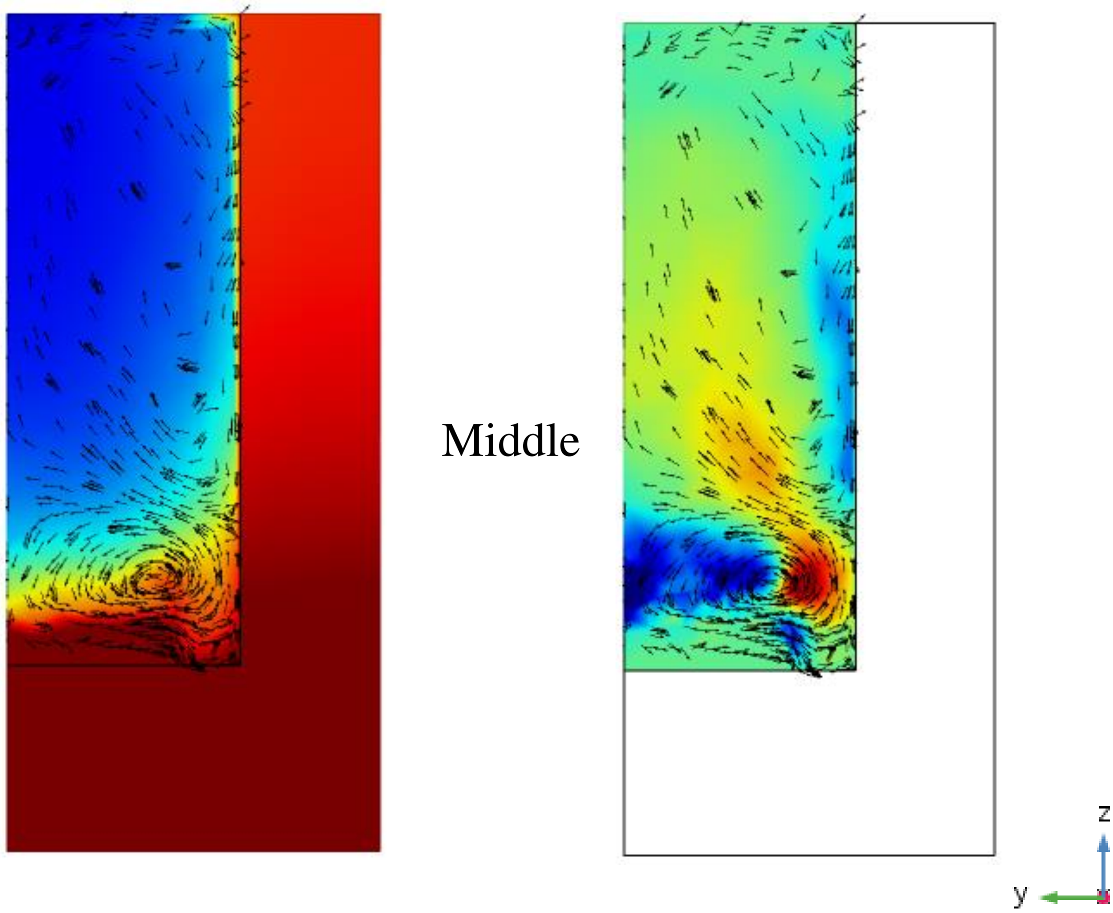

(C)

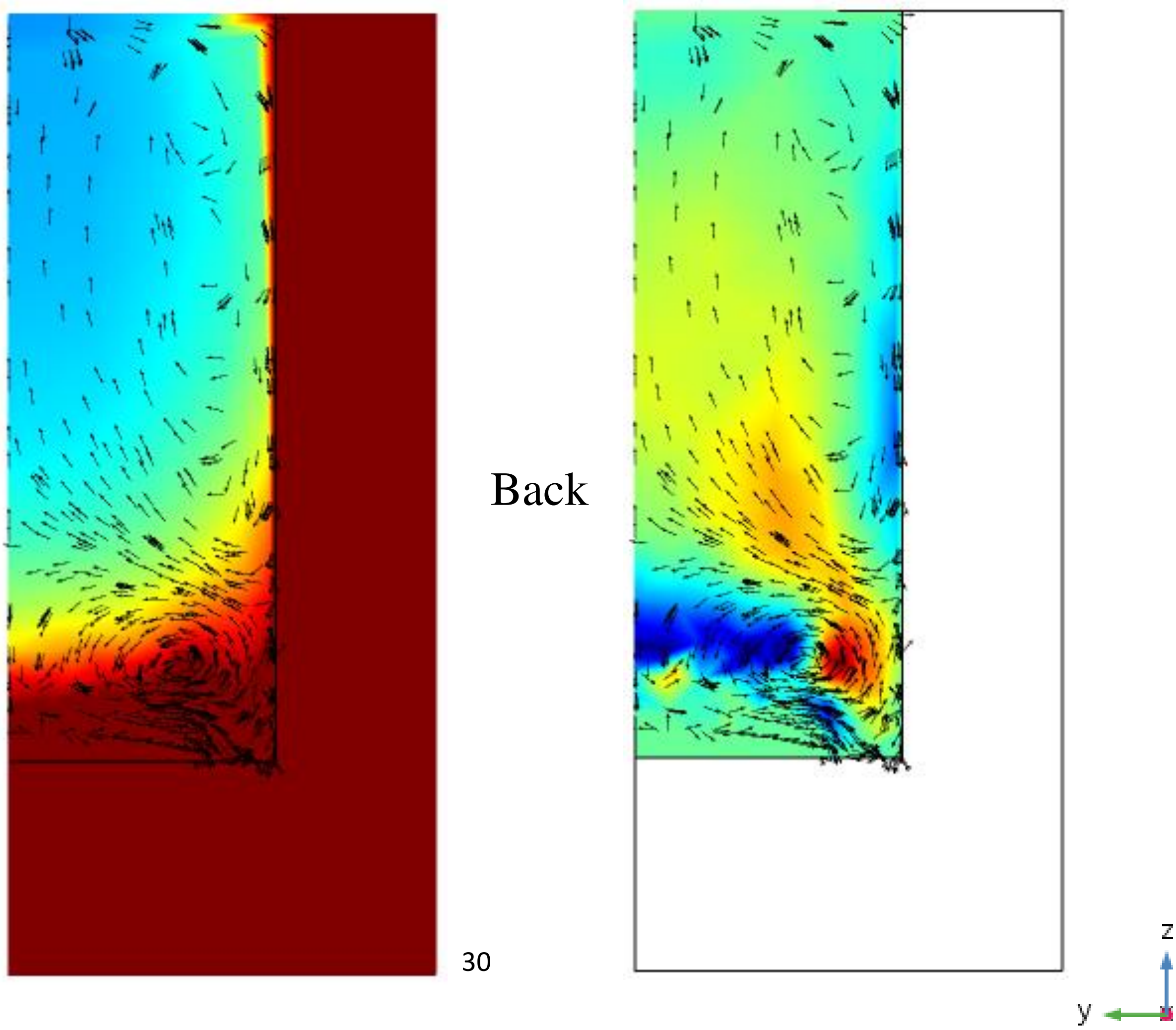

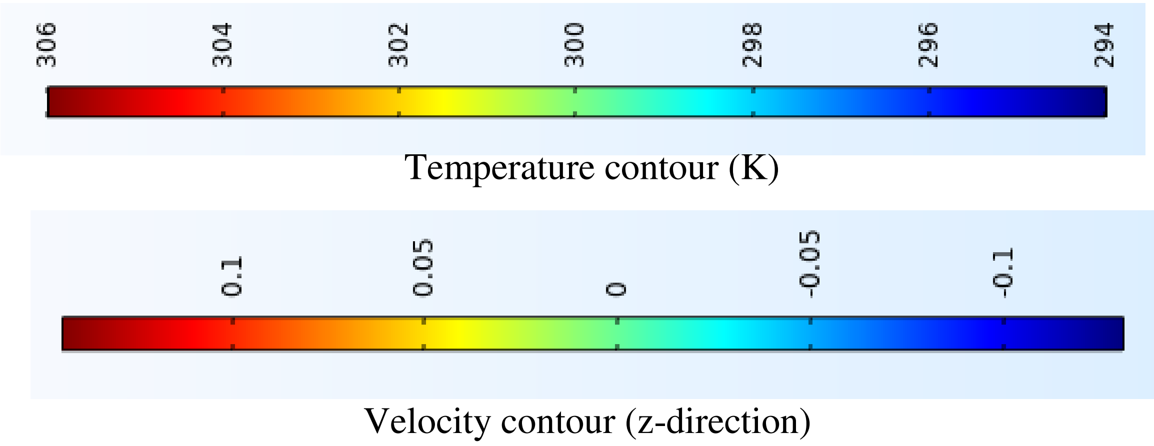

Figure 12: Temperature contours (K) (left side plot) and velocity contours (ms^{-1}) in z-direction (right side plot); (A) front (B) middle and (C) back.

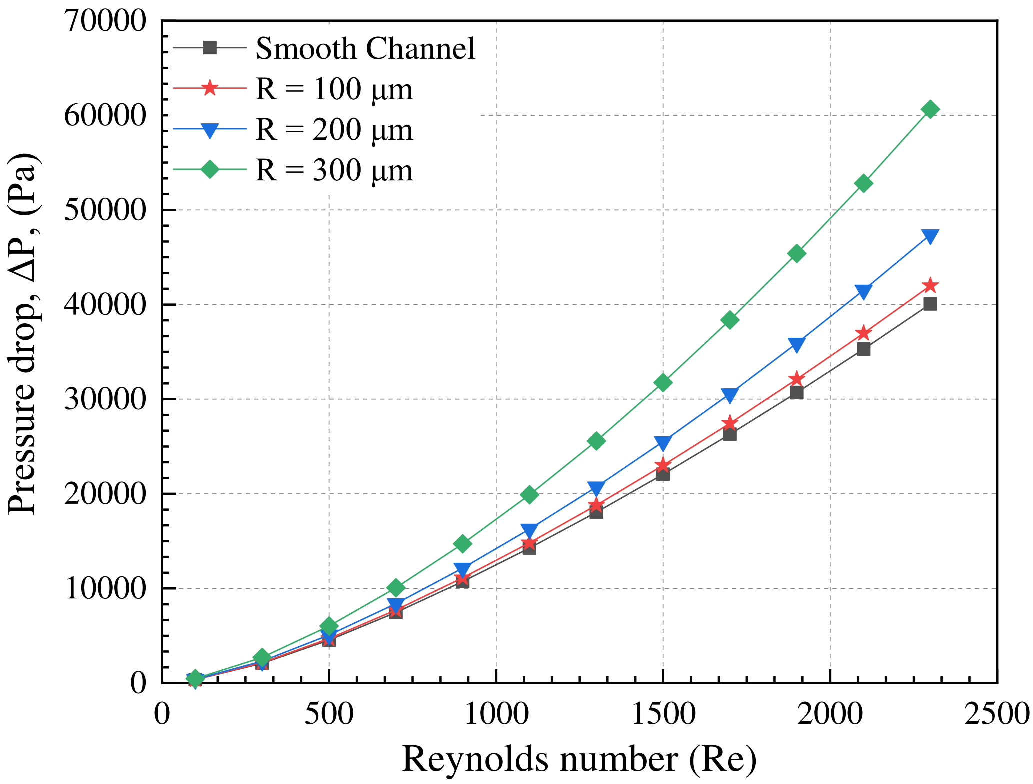

Figure 13: Pressure drop against Re from 100 to 2300 and at the front position with the distance between VGs of 0μm.

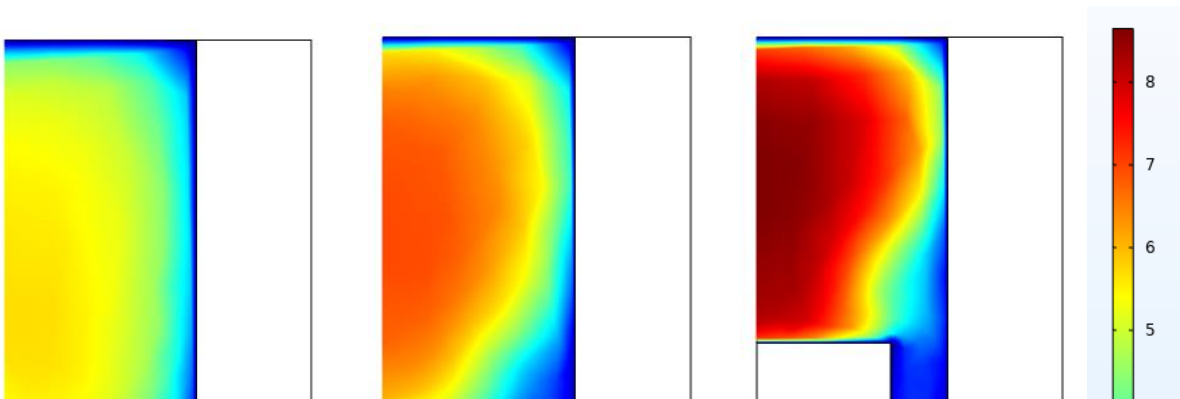

Figure 14: The y-z cross section of the MCHS, with velocity contours (m/s) at different radii of 100μm, 200μm and 300μm at distance between VGs of 0μm for the front position.

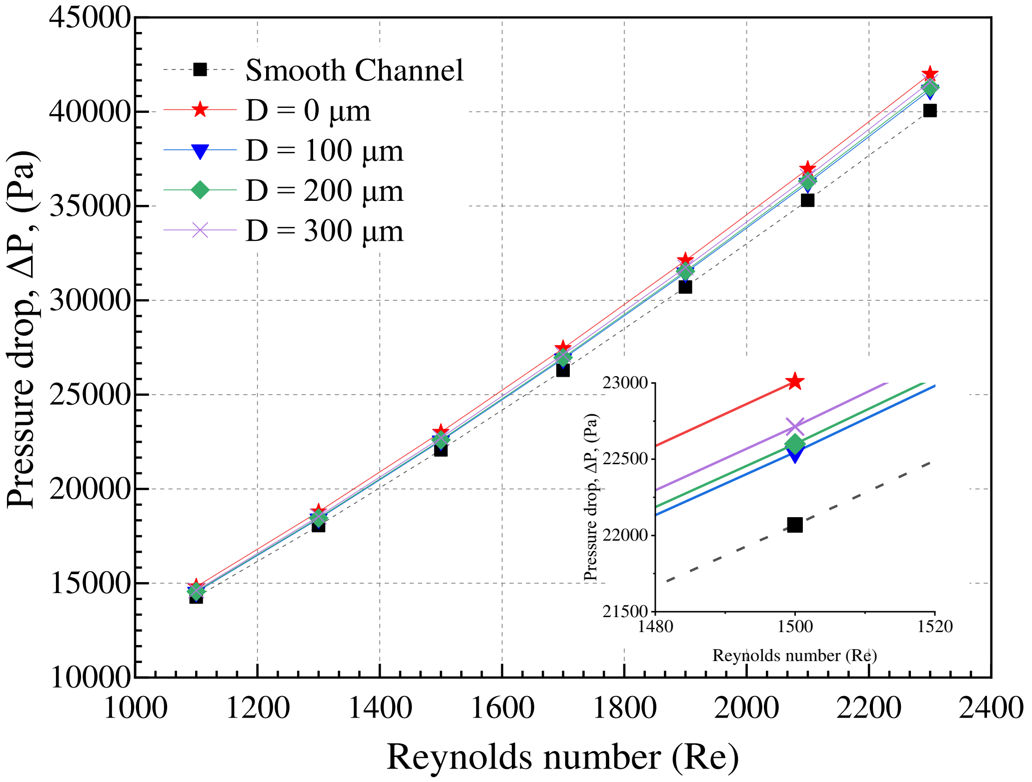

Figure 15: Pressure drop against Re at every distance between VGs ranging from (0-300) μm for the front position at R = 100μm with zoomed in view.

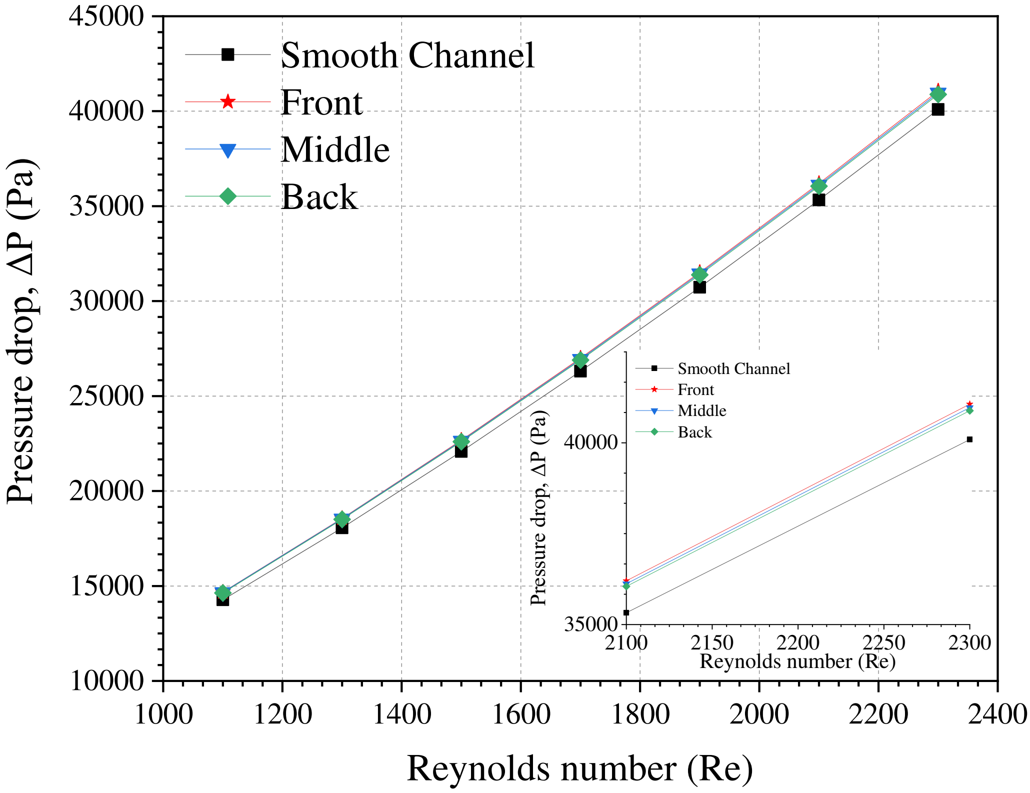

Figure 16: Pressure drop for VGs placed at the front, middle and back with zoomed in view.

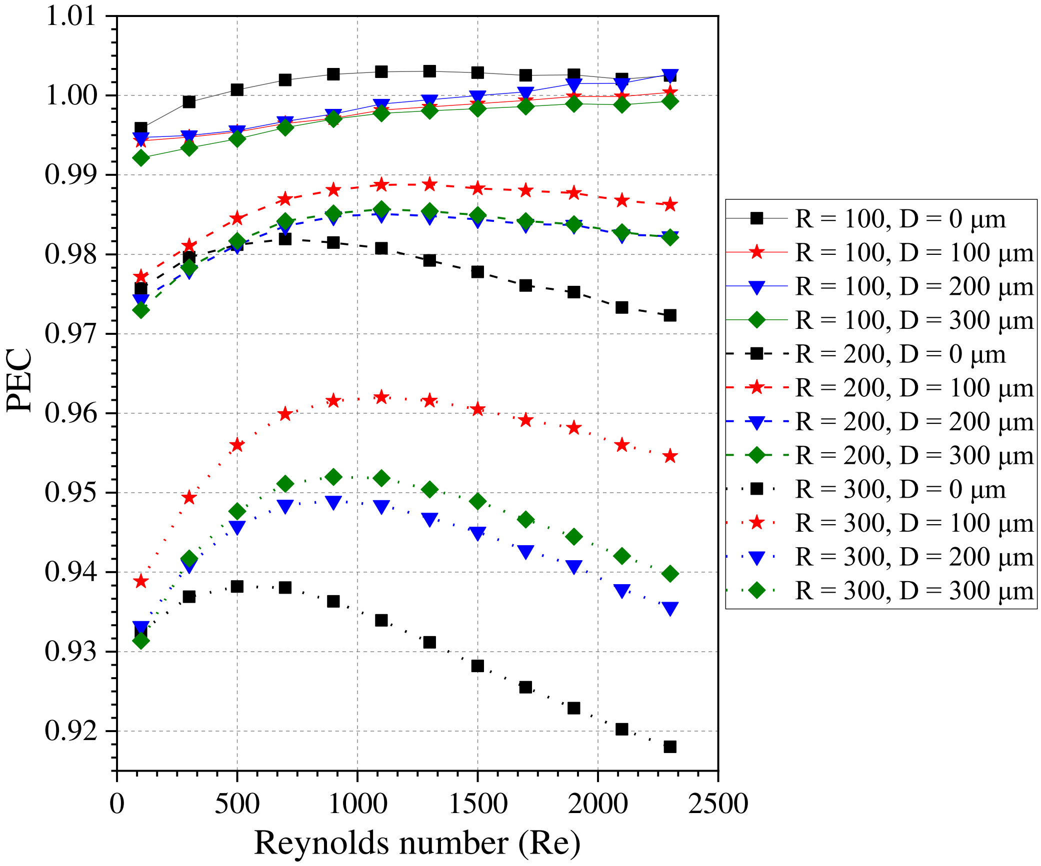

Figure 17: PEC index for different radii and distance between VGs of 0μm, 100μm, 200μm, and 300μm at the front position.

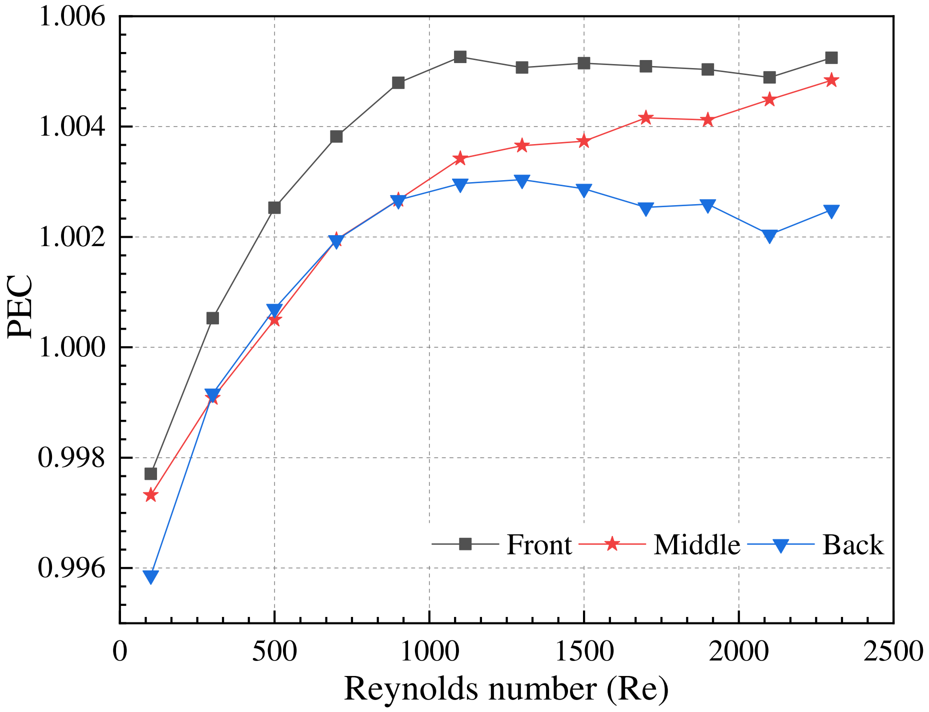

Figure 18: PEC index of different arrangements of VGs (front, middle and back) against Re with the boundary limit set to be 1 for a uniform channel.

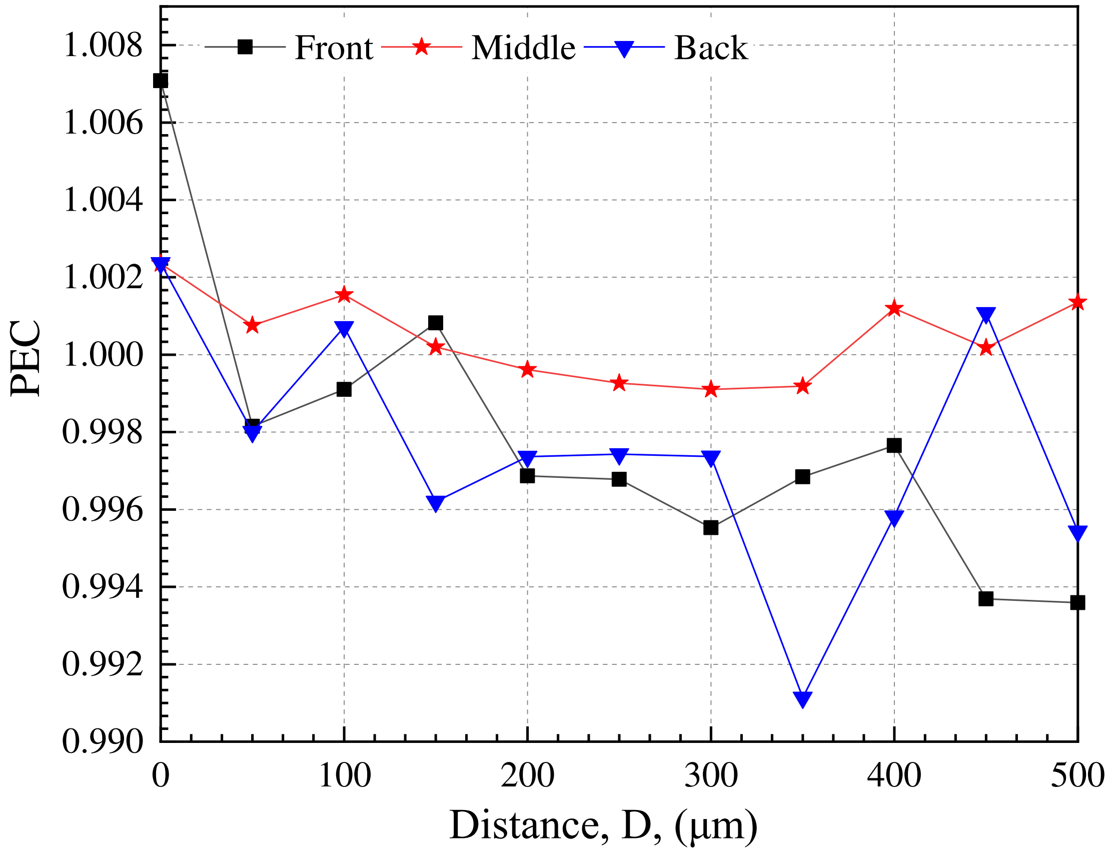

Figure 19: PEC index plot against the distance between VGs at Re= 900 for the three positions.

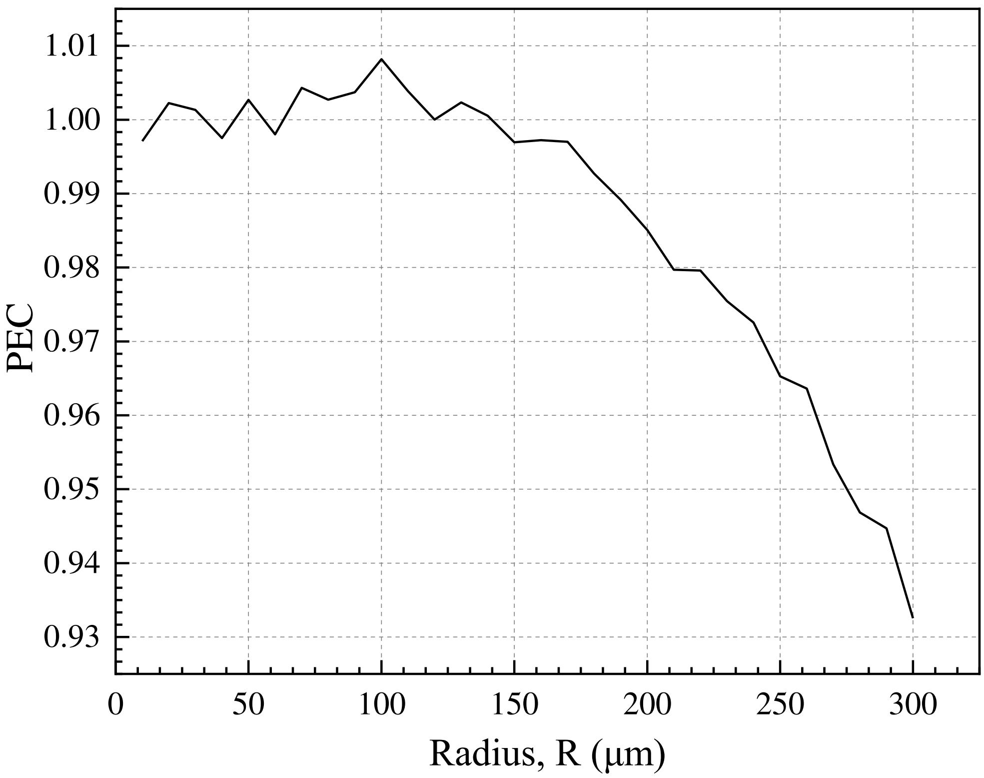

Figure 20: PEC index for increasing radii at constant Re of 900 with distance, D = 0μm at the front position.